Electron Charge Misidentification in the ATLAS Detector

Diplomarbeit

vorgelegt der

Fakultät für Physik
Ludwig-Maximilians-Universität München

von
Michael Wichmann
geboren in München

München, den 25. November 2008

Erstgutachter:	Prof. Dr. Dorothee Schaile
Zweitgutachter:	Prof. Dr. Martin Faessler

Contents

1 Introduction **1**

2 The LHC and ATLAS **3**
2.1 The Large Hadron Collider at CERN . . . 3
2.2 The ATLAS Detector at the LHC . . . 4
2.3 Particle Identification and Reconstruction at ATLAS . . . 8
2.4 Coordinate System and Units . . . 9

3 Detector Components Relevant for Electron Reconstruction **11**
3.1 The Inner Detector . . . 11
3.1.1 The Pixel Detector – Pixels . . . 11
3.1.2 The Silicon Tracker – SCT . . . 12
3.1.3 The Transition Radiation Tracker – TRT . . . 13
3.1.4 The Magnet System . . . 14
3.2 The Electromagnetic Calorimeter System . . . 15

4 Software Tools **19**
4.1 ATLAS Computing Overview . . . 19
4.1.1 Data Formats . . . 19
4.1.2 Tier Structure . . . 20
4.1.3 The ATHENA Framework . . . 21
4.1.4 The Grid and the Grid Interface Ganga . . . 22
4.2 N-Tuple Making . . . 23
4.2.1 The N-Tuple Maker EventView . . . 23
4.2.2 ATHENA Tool for Writing Out GEANT Monte Carlo Electrons . . . 23
4.3 N-Tuple Analysis in Root . . . 24

5 Electron Charge Misidentification **27**
5.1 Electron Reconstruction and Charge Identification . . . 27
5.1.1 Ingredients to Electron Reconstruction . . . 27
5.1.2 Track-Based Electron Reconstruction . . . 27
5.1.3 Calorimeter Cluster-Seeded Electron Reconstruction . . . 29
5.1.4 Important Variables in Electron Reconstruction . . . 29
5.1.5 Quality Criteria for Reconstructed Electron Candidates . . . 31
5.1.6 Determination of the Charge of the Electron . . . 32
5.2 The Issue of Charge Misidentification . . . 33
5.2.1 Electron Charge Misidentification in Simulated Data . . . 33
5.2.2 Matching Monte Carlo Electrons to Reconstructed Electrons . . . 33
5.2.3 Electron Charge Misidentification in Actual Data . . . 34

5.3 Electron Charge Misidentification in Z→ee, ttbar and Single Electron Datasets . . . 34
5.3.1 The Datasets . . . 34
5.3.2 Eta dependence of Charge Misidentification Probability . . . 35
5.3.3 Dependence of Charge Misidentification Probability on Transverse Momentum . . . 37
5.3.4 Electron Author and Charge Misidentification Rate . . . 37

6 Charge Misidentification through Bremsstrahlung and Conversion 41
6.1 Bremsstrahlung and Conversions in Monte Carlo . . . 41
6.1.1 Bremsstrahlung and Charge Misidentification . . . 41
6.1.2 Reconstruction Track Multiplicity . . . 41
6.1.3 A Simple Model for Electron Charge Misidentification . . . 43
6.1.4 Where does Bremsstrahlung and Conversion Occur . . . 44
6.1.5 Relative Charge of Close Tracks . . . 45
6.2 The Simple Model for Electron Charge Misidentification revisited . . . 47
6.2.1 E over p – Calorimeter Energy versus Track Momentum . . . 47
6.2.2 Association of Reconstructed Tracks to Conversion Electrons . . . 49
6.2.3 Transverse Impact Parameter . . . 52
6.2.4 Charge Misidentification at Very High Transverse Momentum . . . 55
6.3 Consequences and Possible Countermeasures . . . 58
6.3.1 Cluster Energy over Track Momentum – E over p . . . 58
6.3.2 Transverse Energy around the Electron Cluster – etcone20 . . . 59
6.3.3 Difference between Cluster Phi and Track Phi – deltaPhi2 . . . 60
6.3.4 Energies in Differently Sized Calorimeter Cells – E233/E237 . . . 61
6.3.5 Transverse Impact Parameter – d0 . . . 62
6.3.6 Track Isolation . . . 62

7 Measuring Electron Charge Misidentification 63
7.1 A Simple Tag-and-Probe Method . . . 63
7.2 Tag-and-Probe with Tag Misidentification Rates . . . 65
7.3 Determining the Tag Charge Misidentification Rate . . . 66
7.4 Verification of the Fit Algorithm with a Toy Monte Carlo . . . 69

8 Conclusions 71

Bibliography 73

1 Introduction

For some physics processes it seems not always essential to unambiguously determine the charge of leptons to uniquely identify a certain decay signature since the knowledge of the existence of a lepton per se suffices. For other processes however a reliable charge identification can be a powerful instrument to discriminate the signal from the background events. A current example would be a decay channel for supersymmetric particles into a final state with two same-sign leptons. A major background for this signal are top-anti-top ($t\bar{t}$) events, with a decay signature resembling the jet rich supersymmetric decay except for the two leptons carrying an opposite charge with respect to each other. Since electrons and muons require quite distinct analysis approaches this thesis will only investigate the issue of charge misidentification for electrons.

From a physics analysis point of view one is primarily interested in electrons coming directly from primary parton collisions. During the passage of the decay products through the detector however, secondary electrons might be created through bremsstrahlung and conversion, complicating the reconstruction of the original electrons.

Chapter 2 gives a brief general overview of the Large Hadron Collider (LHC) and the ATLAS experiment and introduces basic concepts of particle detection and identification.

Chapter 3 contains a more detailed but still non-exhaustive review of the ATLAS Inner Detector components, the magnet system and the electromagnetic calorimeter. These are the detector elements that are relevant to a reliable electron identification and reconstruction. The Inner Detector provides information on the tracks of charged particles. Together with the data from the electromagnetic calorimeter this reveals information about the energy and position of an electron and allows to discriminate electrons from other types of particles.

Modern particle physics does rely heavily on a strong computing infrastructure, encompassing both hardware and software. The ATLAS experiment is no different. The basic organization of computing resources as well as common software tools are discussed in *chapter 4*.

Chapter 5 gives a more in-depth introduction to the ingredients involved in electron identification and particular in charge identification. It will investigate some basic properties of electron charge misidentification found across different Monte Carlo physics data samples.

The importance of bremsstrahlung and conversion processes for electron charge misidentification is discussed in *chapter 6*. Some possibilities to reduce the rate of charge misidentification are pointed out and investigated with Monte Carlo simulation data.

Finally, *chapter 7* takes a look ahead and investigates the possibility of measuring the electron charge misidentification rate in real data.

2 The LHC and ATLAS

2.1 The Large Hadron Collider at CERN

The Large Hadron Collider, LHC for short, is a circular particle accelerator located near Geneva, Switzerland, at the European Organization for Nuclear Research, CERN, formerly known as the "Conseil Européen pour la Recherche Nucléaire". The accelerator is located in a tunnel about 100 m below ground level with a total circumference of about 28 km. At the LHC two proton beams running in opposite directions are brought to collision at several points, where the detectors of the different experiments are located. The LHC is designed for a center of mass energy of 14 TeV, which is more than seven times higher than at the Tevatron at Fermilab near Chicago, which is currently the collider with the highest center of mass energy of 1.96 TeV.

The two proton beams collide at a rate of 40 MHz. A very important design parameter for particle colliders is their luminosity L. Together with the cross section, σ, of a certain process it is a measure for the expected rate, $\dot{N}$, of that process:

$$\dot{N} = \sigma \cdot L \tag{2.1}$$

The luminosity is given by

$$L = \frac{n_1 n_2 f}{4\pi\sigma_x\sigma_y}\,, \tag{2.2}$$

where σ_x and σ_y describe the lateral extent of the two bunches and n_1 and n_2 are the number of particles within each bunch and f the interaction rate. The LHC has a design luminosity of $10^{34}\,\mathrm{cm}^{-2}\,\mathrm{s}^{-1}$. At the LHC design energy the total cross section for proton-proton collisions is almost 100 millibarn, which results in a total of about 10^9 interactions per second. The biggest contribution to this total cross section is however made up of inelastic proton-proton scattering. Cross sections of interesting electroweak interactions are several orders of magnitude below this value. Therefore the challenge for each detector experiment is to filter out the interesting events form this vast number of total interactions and bring down the high number of events to a manageable number for further processing and storage. In the ATLAS detector experiment this is accomplished by a system of triggers and event filters, which will be described in section 2.2.

The counter-rotating beams in the LHC tunnel are guided within the so-called beam pipe. The protons are kept on track by a high number of superconducting magnets that are located around the beam pipe along the whole accelerator ring. Within the beam pipe a very high vacuum has to be maintained in order to avoid losses through beam-gas interactions along the way around the accelerator. A major undertaking is the cooling of the superconducting magnets, which is accomplished by actually cooling almost the whole inner perimeter of the vessel containing the two beam pipes, which has a diameter of more than 50 cm and is filled with an iron core into which the beam pipes and magnets

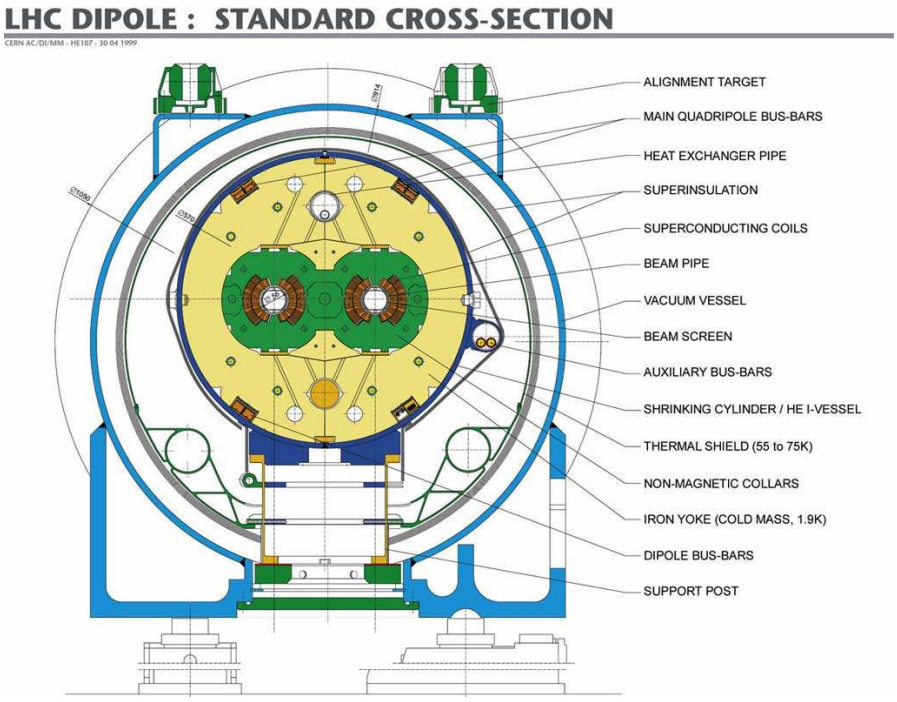

Figure 2.1: Standard cross section of a LHC dipole. The two beam pipes for the two counter-rotating beams are enclosed within a vacuum vessel with a diameter of more than 50 cm. For cooling the beam pipes and superconducting magnets are embedded in an iron yoke, which is kept at a temperature of 1.9 K [1].

are embedded. The so-called iron yoke is kept at a temperature of 1.9 K, by means of a heat exchange pipe running through it. The standard cross section of a LHC dipole is shown in figure 2.1.

Figure 2.2 shows a representation of the CERN accelerator complex. The LHC ring is the last in a complex of particle accelerators. The protons for the LHC are initially accelerated at a linear accelerator (LINAC 2) to about 50 MeV corresponding to a velocity of about $0.3c$. They are then further accelerated in the Booster before being injected into the Proton Synchrotron (PS) at energies of about 1.4 GeV. At the time of injection into the Super Proton Synchrotron (SPS) the protons have reached an energy of about 28 GeV. The SPS then gives the protons a final acceleration to an energy of 450 GeV, at which they are finally injected into the LHC ring in both a clockwise and counter-clockwise direction of circulation. At the LHC ring the final center of mass energy of 14 TeV is reached and the proton beams are brought to collision at four points, one of them being at the site of the ATLAS experiment.

2.2 The ATLAS Detector at the LHC

ATLAS is an acronym for “A Toroidal LHC Apparatus” and is one of the two large all-purpose detectors at the LHC. The overall physical dimensions are impressive. The

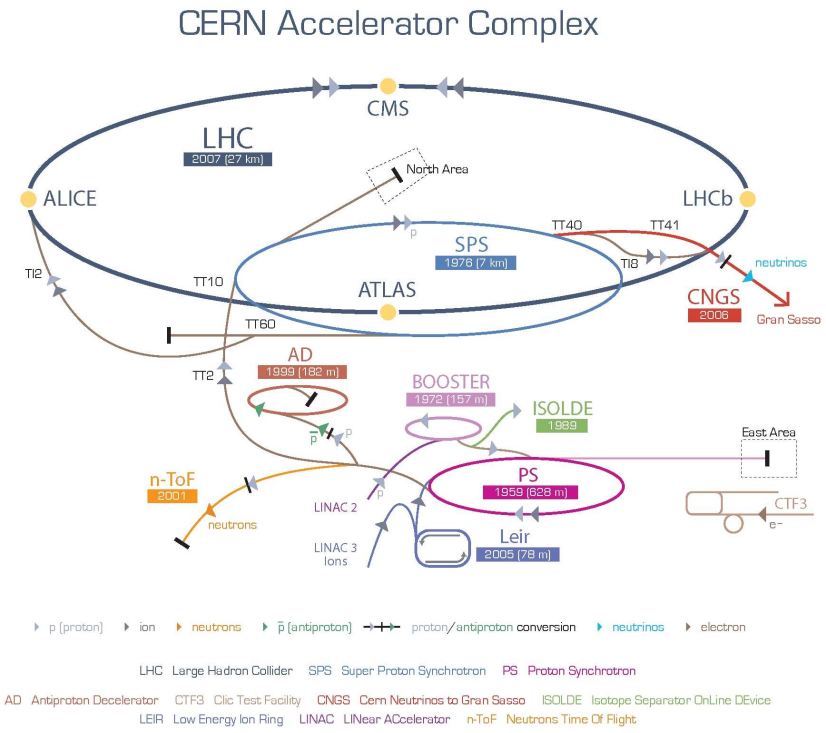

Figure 2.2: The CERN accelerator complex. The LHC is the last ring (dark blue line) in a complex of particle accelerators. The smaller machines LINAC 2, Booster, PS and SPS are used in a chain to help boost the particles to their final energies [2].

total diameter is about 25 m and the total length is 46 m, resulting in a structure with a total weight of about 7000 t. The ATLAS detector is a multi-purpose detector and consists of several standard elements for particle detectors. The basic configuration from inside out is:

- Tracking detectors (Pixel detector, Silicon Tracker, Transition Radiation Tracker)
- Electromagnetic calorimeter
- Hadronic calorimeter
- Muon spectrometer

In addition there are two magnet systems present, one solenoid to provide the magnetic field for the Inner Detector, i.e. the tracking detectors, and a set of toroids, which provide the magnetic field for the muon system. The presence of a magnetic field is necessary to determine the momenta of charged particles from the curvature of their tracks within the magnetic field. This basic arrangement is shown in the schematic view of the ATLAS detector in figure 2.3.

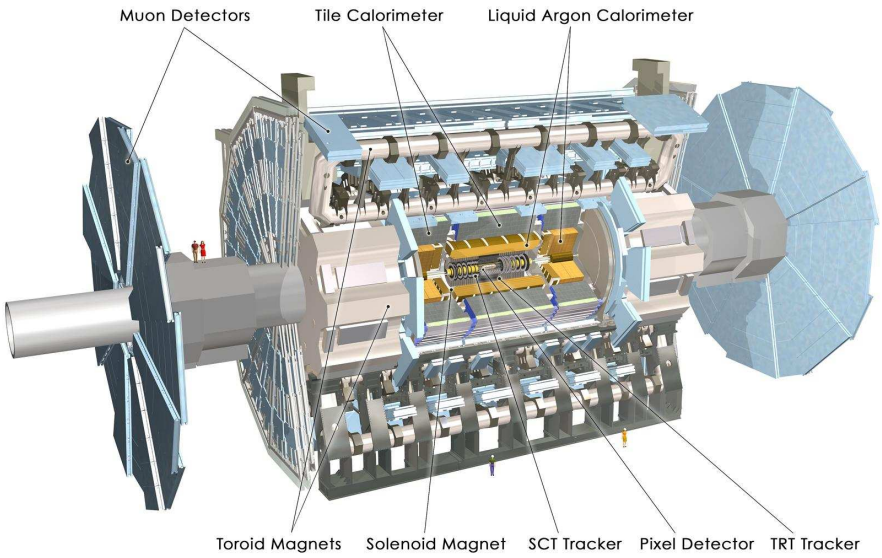

Figure 2.3: Basic layout of the ATLAS detector. The main functional components are labeled. The innermost components are the Pixel, SCT and TRT Trackers followed by the solenoid magnet, which make up the Inner Detector. The electromagnetic liquid-argon and the hadronic tile calorimeters are located just outside the Inner Detector. The final components are the toroidal magnet system, providing the magnetic field for the muon detectors as the outermost components of the ATLAS detector. [1]

The tracking detectors consist of three sub-detectors, the Pixel detector, the Silicon Tracker (SCT) and the Transition Radiation Tracker (TRT). The purpose of the tracking detectors is to determine the track of charged particles traversing the detector. Charged particles leave ionization trails which can be detected by different technologies. While the Pixel detector and the Silicon Tracker are semiconductor detectors, the Transistion Radiation Tracker is made up of thin proportional chambers in the form of straws. The three tracking detectors make up the Inner Detector. The Inner Detector is placed inside a solenoid coil, which provides a mainly uniform magnetic field of about 2 T.

The next active layer of the detector is the electromagnetic calorimeter, which is designed to measure the total energy of electrons and photons by completely absorbing their energy through an electromagnetic shower and measuring the deposited energy. Certainly not only electrons and photons but every interacting particle will leave some energy deposit in the electromagnetic calorimeter. For other particles than electrons and photons this energy deposit is usually small compared to their total energy and they are not completely absorbed by the electromagnetic calorimeter.

After the electromagnetic calorimeter the hadronic calorimeter is placed. This part of the detector is designed to absorb the energy of strongly interacting particles. Due to their higher mass, hadrons will only loose a small amount of their energy in the electromagnetic calorimeter. Their energy is then determined from the sum of the energies deposited in the electromagnetic and hadronic calorimeters.

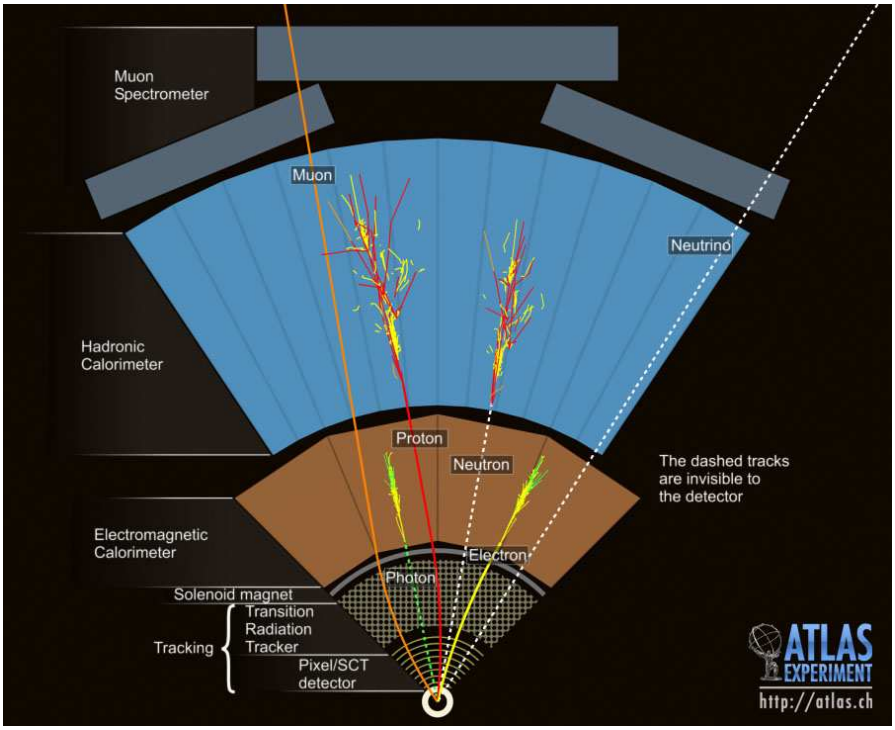

Figure 2.4: Schematic view of several types of particles passing through the ATLAS detector and their typical behavior in the different detector components. [1]

The outermost subsystem of the ATLAS detector is the muon system. It consists of drift tube gas chambers. The muon as a lepton is not subject to strong interactions and due to its high mass of about 106 MeV compared to the electron with a mass of 0.511 MeV, the muon is also much less subject to bremsstrahlung by a factor of $(m_e/m_\mu)^2 \approx 2.5 \cdot 10^{-5}$. Therefore a muon triggering an electromagnetic shower in the electromagnetic calorimeter absorbing the whole muon energy is a very unlikely scenario. Apart from the small energy deposit in the calorimeters the muon energy has thus to be calculated from its track parameters determined in the Inner Detector and the muon spectrometer system. The magnetic field for the muon spectrometer is provided by the toroidal magnet system.

Figure 2.4 shows a schematic view of several particles passing through the ATLAS detector systems. Going from right to left, a neutrino, an electron, a neutron, a proton, a photon and a muon are shown. The neutrino will not interact with any part of the detector and thus be invisible. A neutrino can only be approximately reconstructed as a missing energy signature when the topology of an event is known in its entirety. The electron leaves a curved track in the Inner Detector and will deposit its energy in the electromagnetic calorimeter. The neutron, as a particle carrying no electric charge will not leave any track in the Inner Detector but it is subject to strong interaction, thus depositing its entire energy in the calorimeter system, most of it in the hadronic calorimeter. The energy of a proton will also be detected by strong interactions in the

hadronic calorimeter but in contrast to the neutron it will, as a charged particle, also leave a track signature in the Inner Detector. The photon, electrically neutral, will only be detected as an energy deposit in the electromagnetic calorimeter, leaving no track in the Inner Detector. The muon, as it was mentioned above, will pass most detector components with only a small energy loss. It will however leave an ionization trace, which is used to determine the track of the muon. The properties of a muon must be derived mainly from its track and from a small energy deposit in the calorimeters.

2.3 Particle Identification and Reconstruction at ATLAS

Section 2.1 about the LHC stated that at its design luminosity of $10^{34}\,\mathrm{cm}^{-2}\,\mathrm{s}^{-1}$ and a bunch crossing rate of 40 MHz the LHC will produce events at a rate of about $10^{9}\,\mathrm{s}^{-1}$. It is technically impossible to fully reconstruct and store each event and moreover only a small fraction of the events are of real interest to physicists.

The reduction of the data rate and the selection of potentially interesting events is accomplished by the ATLAS trigger and event filter system. The trigger system is organized in several logical layers or levels. The first layer is the so-called level 1 trigger. It is purely realized in hardware since it has to cope with an interaction rate of about 1 GHz at a bunch crossing rate of 40 MHz. The level 1 trigger only uses calorimeter and muon tracking information at a coarser granularity than the detector is capable of. It triggers on high-p_T objects and defines so-called regions of interest (ROI) for lepton and jet candidates at a certain energy threshold. These regions of interest are spatial regions within the detector that are considered interesting enough to be further investigated by the level 2 trigger. The level 1 trigger reduces the data rate to about 75 kHz. The time between two bunch crossings is 25 ns. The level 1 trigger consists of 100 processing pipelines, so there is a time constraint of about 2.5 μs for each pipeline unit to complete processing. The level 2 trigger then further reduces the event rate to 1 kHz within 10 ms. The level 2 trigger is only looking at the regions of interest provided by the preceding trigger stage. It is now however possible to use the full granularity available from the detector. The data from the regions of interest make a contribution of only about 2% to the total data for one event, therefore drastically reducing the required amount of data to be transferred. The level 2 trigger is implemented in software allowing for greater flexibility. The last layer in the trigger system is the Event Filter. The Event Filter is also purely implemented in software and reduces the event data rate further down to 200 Hz. The event data is then buffered and finally written to disk. The Event Filter has access to the whole event and not only to the regions of interest. At the data rates involved at the Event Filter level the use of more complex reconstruction algorithms is possible.

The data passing the Event Filter is then stored at the computing facilities at CERN and fed into offline reconstruction. Since the data is in permanent storage, there is no tight time constraint to consider in offline reconstruction. Offline reconstruction consists of a complex set of algorithms that are run on the detector data. Two very important tasks, which are of supreme interest to electron identification that offline reconstruction accomplishes are the reconstruction of tracks and the reconstruction of calorimeter clusters. Tracks are fitted based on the information about the hits within the Inner Detector

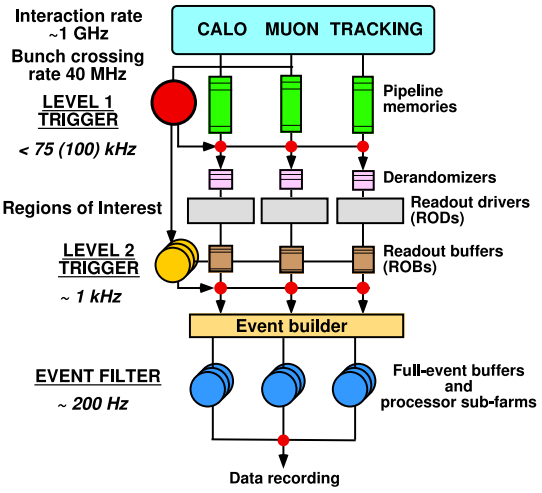

Figure 2.5: Schematic overview of the ATLAS trigger system. Several trigger stages are used to reduce the initial interaction rate to 200 events per second [3].

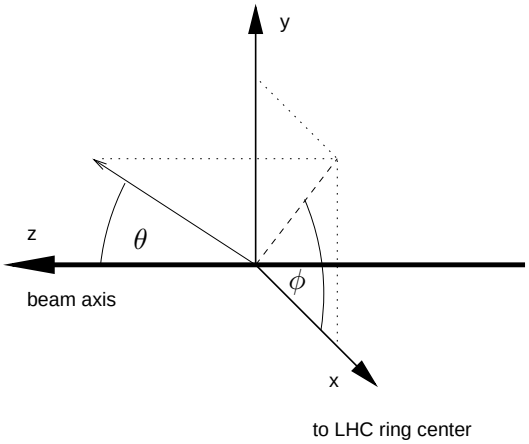

Figure 2.6: The ATLAS coordinate system. The direction of a particle is unambiguously specified by the two angles η and ϕ.

also considering a lot of variables such as misalignment or other calibration data. The fitted tracks are then stored as a track collection in the reconstruction data files. For most conceivable cases of physics analysis there is then no need to go back to the level of discrete tracker hits. Similarly calorimeter clusters are formed from the information on individual calorimeter cells and stored as a cluster collection in the reconstruction data files. During offline reconstruction it is further attempted to associate the tracks to the objects from the calorimeters or tracks from the muon spectrometer system. This is the way electrons are reconstructed as a combination of calorimeter clusters and Inner Detector tracks. Offline reconstruction also tries to reconstruct more complex objects that are a result of a collision event, but already decay within the detector and only the decay products are detected, such as the τ. The goal of the offline processing is to provide a view of the event that is as complete as possible and that is readily usable for most physics analysis purposes. The data is then ready for distribution among the ATLAS community. Most use cases do not contain the need for reprocessing, i.e. rerunning the reconstruction chain by individual physicists in order to perform their analyzes.

2.4 Coordinate System and Units

In order to be able to unambiguously describe the position of detector components and reconstructed objects in the detector it is necessary to define a common coordinate system to be used. For the ATLAS detector the following definitions are made: The direction of the z-axis is defined along the direction the particle beam, thus the x-y plane is defined as the plane transverse to the beam direction. The half-line connecting the interaction point with the center of the LHC collider ring defines the positive half of the x-axis. The positive y-axis is defined as pointing upwards from the interaction point.

Together this then defines the direction of the positive z-axis in a standard right-handed coordinate system as shown in figure 2.6. With these definitions at hand a spherical coordinate system is unambiguously defined. The azimuthal angle ϕ is measured around the beam axis starting at the x-axis and the polar angle θ measures the angle from the beam axis [3].

Another quantity commonly used instead of the angle θ is called the pseudorapidity, denoted by η. The pseudorapidity is defined as

$$\eta = -\ln\left[\tan\left(\frac{\theta}{2}\right)\right] . \tag{2.3}$$

In the ultra-relativistic limit the pseudorapidity η is numerically the same as the rapidity as defined in Special Relativity. The advantage of using the pseudorapidity over the angle θ is due to the fact that the difference in the rapidity of two particles is independent of a Lorentz boost along the beam axis. In hadron colliders the momentum along the z-axis is not easily controlled. At high energies colliding protons will lead to hard interactions between the proton constituents, the quarks and gluons, called partons. Each of these partons will carry a fraction of the total proton momentum. The probabilities of a parton carrying a certain fraction of the proton momentum is described by the *parton distribution function* (pdf). Even if the center of momentum for the colliding protons is at rest, the center of momentum of the interacting partons does not need to be. Interacting partons carrying different fractions of energy of their proton will lead to final state particles that are boosted along the z-axis. Therefore the pseudorapidity η is naturally preferred over the angle θ. Quantities are often only defined in the transverse plane such as the transverse momentum p_T or the transverse energy E_T [3].

The units used throughout this thesis are natural units unless stated otherwise. In natural units the speed of light c, and Planck's constant $\hbar$ are chosen to be equal to 1. Energy is measured in units of electronvolt, eV. The unit of mass then is also the electronvolt, since $m = 1\,\mathrm{eV}/c^2 = 1\,\mathrm{eV}$.

3 Detector Components Relevant for Electron Reconstruction

3.1 The Inner Detector

The ATLAS Inner Detector is responsible for the determination of the tracks of the charged particles generated in a proton-proton collision event. A track is determined by its three-momentum and its origin as well as its sign of curvature determining the charge of the particle giving rise to the track.

In order to provide optimal performance over a wide range of η values the Inner Detector is divided into two regions, the *barrel region* and the *endcap region*. As the name suggests, in the barrel region the detector modules are arranged in concentric cylinders around the beam axis and in the endcap region the tracker modules are arranged in disks arranged perpendicular to the beam axis, in order to provide optimal coverage of both the low and high η regions.

Three distinct tracking detectors make up the ATLAS Inner Detector. Starting from the beam axis going to higher radii these are the *Pixel* detector, the *Silicon Tracker* (SCT) and the *Transition Radiation Tracker* (TRT). The setup of the Inner Detector is shown in figures 3.1 and 3.2. The three systems will be briefly discussed in this section. Located just outside the Inner Detector is the ATLAS magnet system. It is nominally not part of the Inner Detector but shall also be briefly reviewed in this section since it is essential for the working of the Inner Detector, providing the magnetic field which leads to curved tracks.

3.1.1 The Pixel Detector – Pixels

The Pixel detector subsystem is the innermost of the three sub-detectors that make up the ATLAS Inner Detector. It covers the complete range of η values between -2.5 and +2.5. As shown in the plan view in figure 3.2 the Pixel detector consists of three layers in two distinct regions, the barrel region and the two end-caps. The arrangement of the Pixel detector modules in the barrel region is done in coaxial staves mounted in parallel to the beam axis and in the end-cap regions in three disk layers perpendicular to the beam axis, in order to provide optimal resolution throughout the whole η range, since the spatial resolution degrades for low incident angles. The overall length of the Pixel detector is about 185 cm and its diameter is about 38 cm, containing a total of 1744 identical pixel sensors with a size of $19 \times 63\,\mathrm{mm}^2$. The total active area amounts to roughly $1.7\,\mathrm{m}^2$ [4, 5]. Each pixel sensor contains 47232 pixels with a nominal size for most of the pixels of $50 \times 400\,\mu\mathrm{m}^2$. The remaining (about 10%) of the pixels have a slightly larger size of $50 \times 600\,\mu\mathrm{m}^2$. Due to chip design requirements it was necessary in some cases to combine two pixels into one readout channel. This leads to a total of 46080 readout channels and allows a direct determination of the position of a hit in the Pixel detector [4].

The ATLAS Pixel detector is a silicon detector. The underlying principle of operation

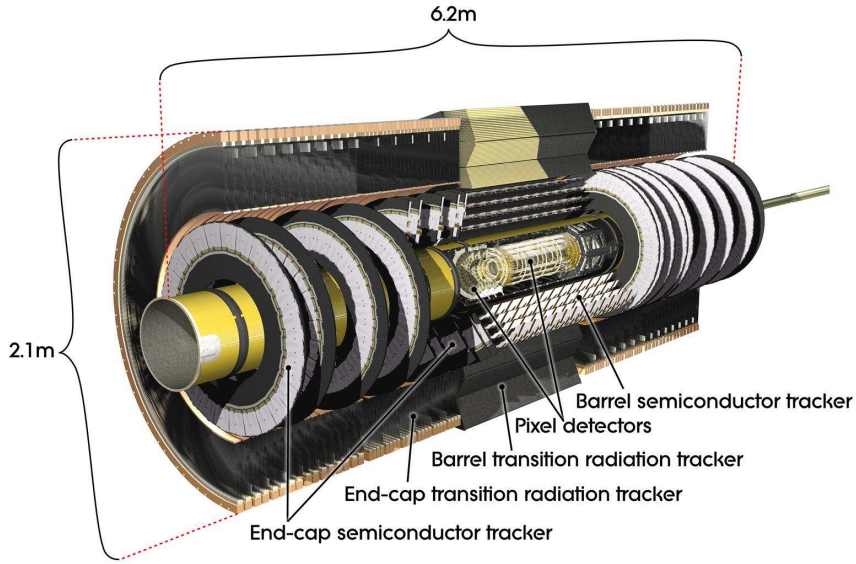

Figure 3.1: Schematic overview of the ATLAS Inner Detector [1].

is based on a p-n junction in reverse bias. Passing radiation will cause the creation of charge carriers, holes in the valence band of the p-doped material and electrons in the conduction band of the n-doped material. The recombination process will lead to a current flow through the p-n junction that is sensed by the readout electronics. Radiation hardness is a major concern with silicon detectors, since the ionizing radiation will lead to an additional doping of the semiconductor material. Therefore the innermost layer of the Pixel detector has an expected lifetime of only three years at design luminosity and will need to be exchanged. The rest of the Inner Detector is designed to last for the entire experiment lifetime of about ten years [4].

3.1.2 The Silicon Tracker – SCT

The Silicon Tracker is based on the same technology as the Pixel tracker. As its name suggests it is also a silicon detector. However, the physical arrangement is different. While the Pixel detector allows a direct determination of the position of a hit due to the very small pixel size, the Silicon Tracker uses a number of sensor chips glued back to back rotated against each other by an angle of 20 mrad or about 1.15°. The sensor chips consist of 768 strips with a length of about 6 cm and a width of less than 80 μm. Two sensor chips are chained together giving an effective strip length of 12 cm. A direct position measurement could thus only yield a spatial resolution of the order of the effective strip size. By arranging the strips back to back with a relative rotation to each other the position of a passing charged particle can be determined with much greater accuracy if it produces hits in both back-to-back sensors. These derived hit coordinates are then called space points.

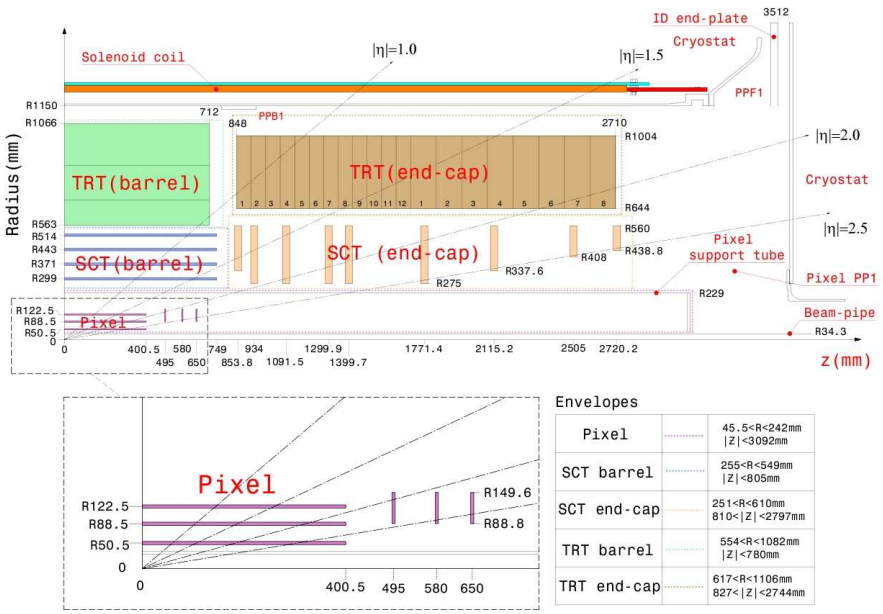

Figure 3.2: Plan view of a quarter-section of the Atlas Inner Detector [4].

3.1.3 The Transition Radiation Tracker – TRT

The Transition Radiation Tracker provides further space points for the determination of track parameters and additionally supports electron identification since it allows the discrimination of particles with different mass. For relativistic particles their momentum dominates the contribution to the particle energy and in the ultra-relativistic limit energy and momentum become of equal magnitude. Therefore it is virtually impossible to discriminate different types of charged particles with only their momentum information from the tracker and the mere energy measurement from the calorimeter. Shower shapes are however different for hadrons and electrons and therefore hadrons are detected mainly in the hadronic calorimeter and electrons in the electromagnetic calorimeter. In addition the Transition Radiation Tracker can yield valuable information on whether a certain track is due to an electron.

Transition radiation is produced when a relativistic particle traverses the boundary of materials with different electromagnetic properties, i.e. with different dielectric constants. The total energy radiated per interface is approximately given by

$$E_{trans} = \frac{2}{3}\,\alpha\,\omega_p\,\gamma\,, \tag{3.1}$$

where α is the fine structure constant with a value of about 1/137, ω_p is the plasma frequency of the radiator material and γ is the Lorentz factor of the particle. The Lorentz factor γ depends on the total energy E of the particle and on its rest mass m_0:

$$\gamma = \frac{E}{m_0}$$

E_{trans} depends linearly on γ, thus the total radiated energy from transitioning electrons will be in the x-ray region, while heavier particles will not lead to high energetic transition radiation. For electrons with an energy from 1 GeV to 100 GeV the emission spectrum typically peaks at 10 keV to 30 keV, with an average number of photons of the order of $\alpha\gamma$ [6].

The ATLAS Transition Radiation Tracker consists of a barrel and an end-cap part, together covering the absolute η range from 0 to 2.0. The barrel to end-cap transition region is located at $0.8 < |\eta| < 1.0$ (see figure 3.2). In the barrel region the Transition Radiation Tracker consists of 73 layers of straws interleaved with fibers or 160 straw planes interleaved with foils in the end-cap region. The fibers or foils provide the interface surfaces for the transition radiation, while the emitted x-ray photons are detected within the drift-tubes, the straws. The straws are filled with a Xenon, CO_2, O_2 gas mixture. All charged tracks with a transverse momentum p_T greater than 0.5 GeV and $|\eta|$ less than 2.0 will traverse at least 36 straws except in the barrel to end-cap transition region, where still at least 22 straws are crossed. The readout electronics distinguishes between low and high threshold hits, where high threshold hits are expected for the transition radiation coming from electrons. There are typically 7 to 10 high threshold hits expected for an electron with an energy greater than 2 GeV [4].

3.1.4 The Magnet System

Though not nominally part of the Inner Detector the magnet system is essential for the functioning of the Inner Detector tracking system, since it is responsible for bending the trajectories of charged particles. By measuring the curvature of the tracks of the charged particles in the Inner Detector trackers, quantities such as the sign of the charge and the transverse momentum p_T can be directly measured. The ATLAS magnet system consists of four superconducting magnets, one solenoid in the barrel region of the detector and a total of three toroids, one barrel toroid in the central region and one end-cap toroid in each of the two end-cap regions. Figure 3.3 shows a graphical representation of the geometry of the ATLAS magnet system.

The central solenoid is the only part of the magnet system that is of real interest for the Inner Detector, since the Inner Detector is completely enclosed within the solenoid (see figure 3.2) and such only sees the principally uniform field of a long coil. It has an axial length of 5.8 m and an inner diameter of 2.46 m. The central solenoid is designed to provide a 2 T axial field within the Inner Detector cavity. Figure 3.4 shows the measured radial and axial magnetic field components within the Inner Detector cavity. For small distances from the center of the detector the measured field actually consists of virtually only a 2 T axial field component. Proceeding further to the ends of the solenoid the radial component of the magnetic field increases, while the magnitude of the axial component decreases. These distortions of the uniformity of the magnetic field within the Inner Detector are stored in a database and are read out and taken into account during the process of track fitting by the reconstruction software algorithms [4, 7].

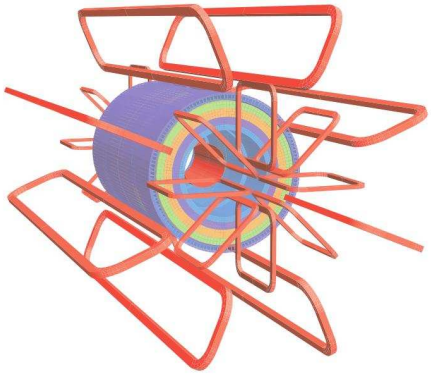

Figure 3.3: Geometry of the magnet system of the ATLAS detector. It consists of one solenoid in the barrel region and three toroids, one barrel toroid in the central region and one end-cap toroid in each of the two end-cap regions [4].

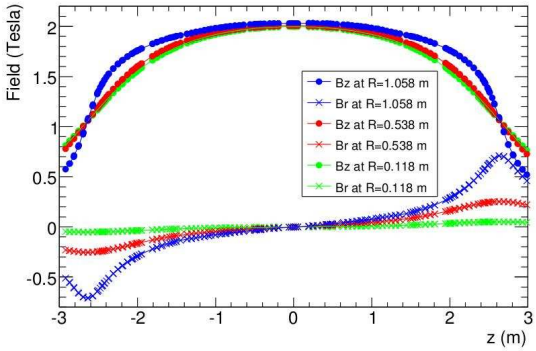

Figure 3.4: Measured radial (B_r) and axial (B_z) magnetic field components within the Inner Detector cavity versus z for different distances R from the beam axis [4].

3.2 The Electromagnetic Calorimeter System

The electromagnetic calorimeter of the ATLAS detector is responsible for measuring the energies of electrons and photons by absorbing their energy through generation of electromagnetic showers. The calorimeter consists of alternating layers of lead plates and gaps filled with liquid argon. Three copper electrodes are embedded in the liquid argon. The two outer electrodes are on a high electrical potential while the middle electrode is connected to the read out electronics. The principle of operation of the electromagnetic calorimeter relies on the properties of interaction of electromagnetic particles with dense matter. The lead absorbers are responsible for creating electromagnetic showers, where the two processes of photon conversion and bremsstrahlung alternate until the resulting particles have low enough energy to be absorbed by the material. The shower constituents then ionize the liquid argon and the argon ions drift within the electric field of the electrodes, creating an electrical current when making contact with the electrodes. The resulting signal is read out through capacitive coupling of the middle electrode and fed into read out electronics.

The lead-electrode sheets of the electromagnetic calorimeter are folded in an accordion shape in order to provide best coverage in the ϕ direction. A sketch of a barrel calorimeter module is shown in figure 3.5 with the indication of the accordion shaped lead sheets. The calorimeter is arranged in a barrel region and two end-cap regions covering absolute η values from 0 up to 3.2. The barrel region consists of two half-barrels from $\eta = 0$ to $\eta = \pm 1.475$ with a length of 3.2 m and an inner and outer diameter of 2.8 m and 4 m respectively, each weighing about 57 t. The end-cap region also is divided into two disks, with diameters of 2098 mm and 330 mm covering the η ranges from 1.375 to 2.5 and 2.5 to 3.2 respectively. The barrel calorimeter covers the η range of up to 1.475, so there is an overlap between the barrel and end-cap calorimeter. The thickness of the

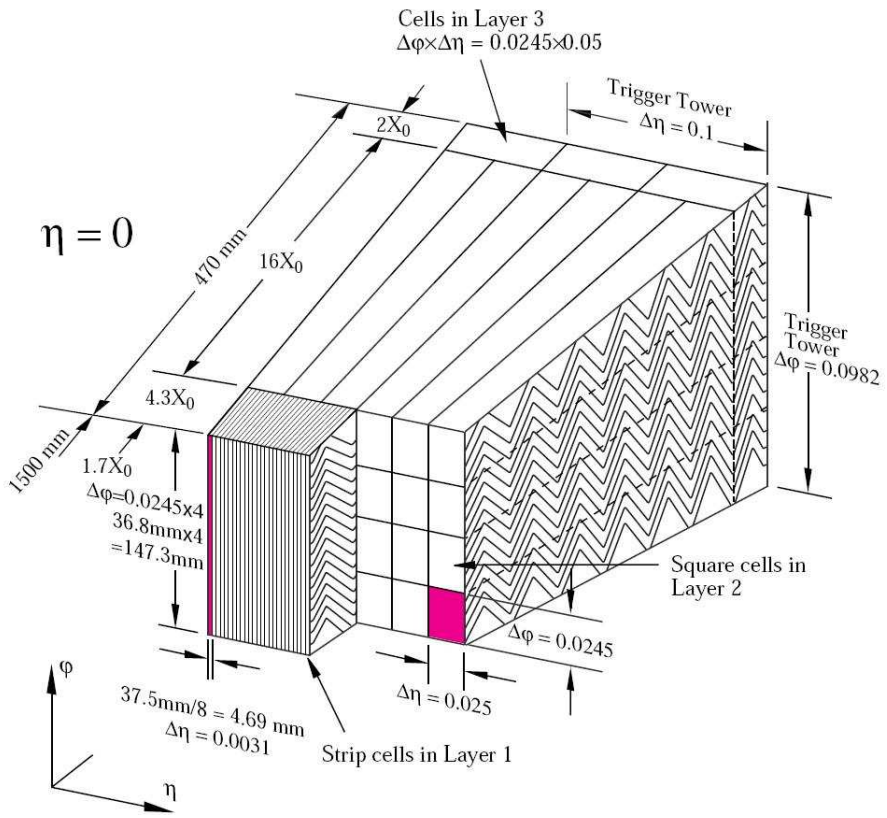

Figure 3.5: Sketch of a barrel module of the electromagnetic calorimeter. The three layers of the calorimeter are shown with their respective radiation lengths [4].

electromagnetic calorimeter in terms of radiation lengths X_0 is always greater than $22X_0$. It ranges from $22X_0$ to $30X_0$ in the η range from 0 to 0.8 and from $24X_0$ to $33X_0$ for $|\eta|$ within 0.8 and 1.3, as well as $24X_0$ to $38X_0$ for $|\eta|$ between 1.475 to 2.5. In the barrel region there are a total of 2048 accordion shaped lead absorbers and in the end-cap region there are each 1024 lead absorbers installed [4].

The calorimeter consists of three distinct layers, sometimes called samplings, with the second layer being the largest absorbing the highest fraction of energy. In the barrel region it has a length of about 470 mm, which corresponds to 16 radiation lengths X_0, so that all but the highest energetic showers are totally absorbed within the middle layer. Particles crossing the lead plates at higher incident angles have to effectively pass through more material. Therefore the thickness of the lead plates is chosen to be either 1.5 mm or 1.1 mm depending on the η position in the detector to compensate for this effect. The middle layer of the electromagnetic calorimeter is arranged in so-called calorimeter cells. Each cell has a dimension of about 0.025×0.0245 (rad) in η and ϕ respectively up to a pseudorapidity of $\eta = 2.5$. The third layer is divided into coarser cells with a dimension of $\Delta\eta \times \Delta\phi = 0.05 \times 0.0245$ and has a thickness of $2X_0$. The first layer and is arranged in so-called strip towers. They provide a very high granularity in

the η direction but extend over several cells of the second layer in the ϕ direction. Their dimensions are $\Delta\eta \times \Delta\phi = 0.98 \times 0.0031$, thus providing a η resolution eight times higher than the second layer. The first layer has a thickness of $4.3X_0$ [4].

All in all the setup of the electromagnetic calorimeter allows a fine measurement of a shower position and lateral shower parameters through the division in the η and ϕ direction. The arrangement in three layers allows to make inferences about the depth of a shower, which is used to discriminate electrons from other types of particles, which usually deposit a considerable amount of energy in the third layer and even the hadronic calorimeter.

The hadronic calorimeter is usually not of very high interest to electron reconstruction, except for the suppression of the reconstruction of fake electrons, i.e. an non-electron object being reconstructed as an electron. Charged pions and particle jets in general do of course leave an energy deposit in the electromagnetic calorimeter. It is attempted to suppress the reconstruction of those objects as electrons by using information on the shower shape. One variable involving the hadronic calorimeter is the so-called hadronic leakage, which describes the amount of energy deposited in the first layer of the hadronic calorimeter compared to the total energy deposit in the electromagnetic calorimeter. For electrons this value usually is very low, since the electron energy is completely absorbed in the electromagnetic calorimeter and should not punch through to the hadronic calorimeter.

An important parameter of the electromagnetic calorimeter is its energy resolution $\Delta E/E$. It can be parametrized as follows:

$$\frac{\Delta E}{E} = \frac{a}{\sqrt{E}} \oplus b\,. \tag{3.2}$$

The expected values of the two parameters are $a = (10.1\% \pm 0.1\%) \cdot \sqrt{\text{GeV}}$ and $b = 0.17\% \pm 0.04\%$. The symbol $\oplus$ indicates that the two terms have to be added in quadrature, e.g. $c \oplus d = \sqrt{c^2 + d^2}$ [8].

4 Software Tools

4.1 ATLAS Computing Overview

The large scale of the ATLAS experiment and the large amount of data generated during data taking requires exceptional efforts for data distribution and analysis. Therefore computing is of greatest importance to the ATLAS experiment. The ATLAS computing infrastructure has to deal with huge amounts of data being produced by the ATLAS detector. After passing through the three-stage trigger system, the frequency at which data has to be recorded is reduced from the initial 40 MHz bunch crossing rate to about 200 events per second. The ATLAS Computing Technical Design Report [9] states expected data sizes per event for different data formats. According to this report the raw data size is expected to be around 1.6 MB per event, which amounts to 160 MB per second having to be stored and subsequently fed into offline reconstruction algorithms. The data has to be distributed among the members of the ATLAS collaboration around the world. In order to be able to manage such a huge amount of data and satisfy the needs of physicists, a computing model has been put in place which ensures a healthy balance between the needs of the users and the resources available. This section briefly discusses multiple aspects of the computing model and its implementation, introduces the ATHENA framework used by the ATLAS experiment and gives a short user centered overview of grid computing, as far as it is of concern for this analysis.

4.1.1 Data Formats

Several data formats are in use within the ATLAS experiment, which contain representations of the recorded events in varying levels of detail.

Raw Bytestream Data – RAW
To begin with, there is the raw data stream that comes from the hardware and software triggers and online reconstruction. In this bytestream format each event occupies about 1.6 MB of space for data storage. The raw data is stored in files of at most 2 GB at CERN computing facilities [9].

Event Summary Data – ESD
The raw data stream is analyzed by offline reconstruction software in order to generate the **E**vent **S**ummary **D**ata, ESD. The ESD is considered the most basic data format to be used for physics analysis. Under normal circumstances it should not be necessary for physicists to access the raw data unless for a review of reconstruction algorithms or for calibration purposes. The storage size is about 500 kB per event. The ESD has an object-oriented representation [9].

Analysis Object Data – AOD
The **A**nalysis **O**bject **D**ata, AOD contains a reduced event representation and is derived from the ESD. Data objects that are not considered necessary for physics analysis are

not copied to the AOD. This format is considered to be the most suitable for actual physics analysis, since the required amount of storage only amounts to about 100 kB per event. Like for the ESD, there exists an object-oriented representation for the AOD data [9].

Derived Physics Data – DPD

Further reduction of event data size is possible and is endorsed by several physics groups within the ATLAS experiment that have agreed on common quantities important for their studies. There exist several flavors of **D**erived **P**hysics **D**ata, DPD. A common approach, which was employed before when going from the ESD to AOD format, is to just include a subset of quantities from the AOD into the generated DPD. This is called *slimming* of the AOD. A different approach is to only select events with certain properties, which is called *skimming* in ATLAS jargon. Another type of DPD is the n-tuple, or D3PD, which is called a flat data structure since it does not have an object-oriented representation anymore but consists of merely a tabular summary of the event data. For many purposes this is the most convenient format to work with in a practical analysis.

Raw Data Object – RDO

Another data format is the **R**aw **D**ata **O**bject, RDO. This format is only used for Monte Carlo generated detector response data. In contrast to the raw bytestream format the RDO has an object-oriented representation and is therefore much more convenient to work with. Offline reconstruction can be run on a RDO.

4.1.2 Tier Structure

The computing facilities of the ATLAS experiment are spread over a number of data processing facilities at different locations throughout the world at the participating institutions. Different facilities are charged with distinct roles, which is represented by the Tier structure. The data is distributed among different sites, while at least two copies of the main data formats must be present in the system to ensure no data is lost in case of failure [9].

Tier 0 at CERN

The computing facility at CERN is the only Tier 0 facility. It is responsible for archiving and distributing the RAW data received from the experiment after passing the Event Filter. It is responsible for the prompt reconstruction of data for calibration purposes and the first-pass processing of the primary event stream, which has a little less stringent timing requirements. The produced ESD and AOD datasets are then distributed to the Tier 1 sites along with the RAW data. The Tier 0 facility does not grant access for analysis purposes. Naturally the highest level of reliability and the shortest response times in case of failure have to be ensured [9].

Tier 1 Sites

There is a total of about 10 Tier 1 facilities. Their role is to host and to provide long-term access to a subset of the RAW datasets received from the Tier 0 facility at CERN. The total amount of raw data will be spread over all Tier 1 sites, so that each is storing

about one tenth of the total RAW datasets. Another main responsibility of the Tier 1 sites will be the reprocessing of the RAW data and to provide access to the derived data formats with a low latency. The ESD data produced at one of the Tier 1 facilities is copied to another Tier 1 facility in order to provide a backup copy in the case of failure. A given ESD dataset is thus available from two different Tier 1 sites, giving reasonable protection from severe data loss. Before the availability of real detector data, the Tier 1 sites will also be committing computing power to the production of Monte Carlo simulation datasets. The requirements on the reliability of the Tier 1 sites are very high. Downtimes of more than 12 hours will be problematic in terms of catching up with processing and storage. The access to Tier 1 sites is restricted since their responsibility is mainly the reconstruction and storage of detector data and not the provision of general analysis capacity [9].

Tier 2 Sites

The Tier 2 facilities provide the main part of computing capacity for data analysis. They will be the only sites in charge of production of simulation data, once real data taking has begun. The produced simulation datasets will however be migrated to the Tier 1 facilities for storage and hosting. A Tier 2 site is intended to host about one third of the available primary AODs in the current version as well as a modest sample of RAW and ESD data. In the case that a user needs to use back-navigation, i.e. needs to access RAW or ESD data for a given AOD, Tier 2 sites are supposed to provide an automated process of copying small amounts of data from the Tier 1 facilities. The Tier 2 sites are also the place for storage of the derived physics data, DPD, for the different physics groups [9].

4.1.3 The ATHENA Framework

The ATHENA software framework [9] is a collection of software code that contains almost all offline computing code of the ATLAS experiment. It contains the reconstruction algorithms, as well as analysis algorithms and even programs for the graphical display of events. The ATLAS Computing Workbook [10] gives a short definition of the term "framework". A framework is thus supposed to provide a skeleton of an application into which developers are integrating their code. It provides a set of common functionality shared by all or a great number of the pieces of code in the framework, thus factoring out common functionality for re-use. By providing a common framework the underlying design philosophy of the software is enforced and a common approach is encouraged. The ATHENA framework is based on the Gaudi software package [11] originally developed by the LHCb experiment. A leading principle of the framework architecture is the abstraction through the stringent use of interfaces. A well controlled and defined abstract interface allows independent development of different pieces of code that communicate with each other through the predefined interface, allowing encapsulation of the actual code. The specific implementation of an algorithm is transparent to the other software components in the framework since communication between different parts of the software takes place only through the defined interfaces. Reconstruction and data analysis requires the handling of large amounts of data. The ATHENA framework makes use of a concept called transient storage for allowing a seamless exchange of data among different

algorithms. One algorithm may be using data from the transient storage as input, which was generated before by another algorithm and written to this transient storage space. This is used for example during data reconstruction. The piece of code that is responsible for finding electron candidates uses information that was previously written by a cluster finder algorithm for the electromagnetic calorimeter and track data that was generated by the track finder algorithms. The different algorithms and processes are not in direct communication with each other but rather exchange data and information through the transient storage space. This way for example it is easy to employ a different track fitter without the need to change anything within the electron reconstruction algorithm itself.

The ATHENA framework makes heavy use of the scripting language Python for program control and sequencing. The actual programs are usually written in the compiled programming language C++. From a user perspective, at the top level there is a so-called job options file, written in Python, that is responsible for loading and calling the appropriate components of the ATHENA framework. Within the job options file the program sequence is defined and custom parameters for the different modules and algorithms are set. Many subpackages within the ATHENA framework come with their own steering and configuration scripts that need to be called from the job options file. This approach makes the whole framework architecture very flexible but sometimes also quite complex from a user perspective.

4.1.4 The Grid and the Grid Interface Ganga

The Grid is a inhomogeneous collection of computing sites that provide computational data analysis services through a common interface. Since the ATLAS experiment is dealing with huge amounts of data it is not possible for every user or working group to store the needed data and run an analysis on it locally. Grid computing allows the code to be sent to the data, where this is the more economical solution. In a previous section the Tier structure of the ATLAS computing facilities was introduced. The Tier 2 sites were said to be required to provide computing capacity for the data analysis. From a simple user perspective the Tier 2 sites make up the Grid. Analyzes are designed locally within the ATHENA framework and can be tested on a very small amount of data. Then the ATHENA job can be submitted to the Grid, where the analysis program is sent to the sites holding the requested data files. Essentially any executable program can be run on any system participating in the Grid. Very low level software tools are present for such a case. However this process can become quite complicated in the case of using ATHENA jobs, since several steps are involved. Firstly, the Grid is a heterogeneous network, so one cannot rely on finding a specified setup on every host site. Operating system and hardware architecture may vary, so a recompilation of some code might be necessary. Secondly it might be the case that a particular dataset is not available on a specific Tier 2 site or that the site is not operational at the moment. Before submitting a job to a site on the Grid it is essential to check if the requested data is available there and whether the site is operational. And last the output data needs to be retrieved. All these steps would result in a tedious and impractical workflow in the case of a simple analysis task.

A great simplification and automation of this process is provided by a software called Ganga [12, 13]. Ganga itself is written in Python and is controlled by a Python script,

which contains the basic information needed to submit an ATHENA analysis job, such as the datasets required, preferred sites to submit to or required software versions. Ganga then takes care of finding the sites holding the required datasets and checking if all requirements are fulfilled. It reports on the status of submitted jobs and in case of failure allows an easy resubmission. The output data created by the submitted job is collected and transferred back, so they are locally accessible.

4.2 N-Tuple Making

4.2.1 The N-Tuple Maker EventView

The ATHENA framework does provide for data analysis tasks, however that is often more easily and flexibly achieved by using other data analysis software packages such as Root [14]. In contrast to ATHENA which is designed to deal with the object-oriented storage data formats such as ESD and AOD, Root operates with so-called flat n-tuples. These are tabular representations of the event data, just like in a relational database. For example for each electron in an event there is one entry in a table, which holds all the attributes of the electron such as energy, transverse momentum, etc. The generation of an n-tuple is achieved within the ATHENA framework. Within the ATHENA framework there are several pieces of software available to accomplish this task, for example HighPtView or the TauDPDMaker. All of these n-tuple makers are based on a collection of ATHENA algorithms and tools which is called EventView. The EventView package provides functionality to loop over each event of a dataset, select events by certain criteria, remove overlap among several reconstructed particles in an event and write out the collected information at the specified level of detail into a Root n-tuple. During reconstruction each electron for example is also reconstructed as a jet. This is called overlap and leads to inconsistencies. It is therefore necessary to make a decision to keep only one of these objects. This overlap can either be removed when creating the n-tuple or has to be removed within the Root analysis code. An important choice when creating n-tuples is the level of detail to be written for each type of particle. This has great impact on the size of the resulting n-tuple. EventView provides several levels of detail, which range from only the kinematic information to the full information contained in the AOD.

4.2.2 ATHENA Tool for Writing Out GEANT Monte Carlo Electrons

The analysis of this thesis makes use of Monte Carlo electrons that were generated during the detector simulation. The full simulation of physics events requires three main steps. First the physical events are simulated, i.e. the particles resulting from a proton-proton collision are generated. Secondly these *generator level* particles are fed into the detector simulation, which calculates the behavior of the particles passing through the detector and simulates the full detector response to these particles. The detector simulation must take into account the fields present in the detector, as well as the physical interaction with the detector material, i.e. bremsstrahlung effects. The software package used for the detector simulation is named GEANT, therefore particles arising from the detector simulation and not from the event generator are sometimes called GEANT particles

in order to distinguish them from particles on generator level. The third step is the reconstruction of the simulated events. The simulated detector response is fed into the same reconstruction algorithms that are used for actual events as if it were real data.

By default, n-tuple makers write out only information on the generator level particles and the reconstruction results. The analysis in this thesis however requires extended information on the electrons generated during detector simulation, the so-called GEANT electrons. In order to write out this information in the produced n-tuples, first the EventView steering script had to be adjusted to include GEANT electrons into the class of selected particles and secondly an ATHENA algorithm had to be developed in C++, which is responsible for gathering the data needed from the input AOD. The particular data items for each GEANT electron are:

- *PDG id*[1] and *barcode*[2] of the generator level parent electron
- Fraction of energy taken from the generator level parent electron
- Production and decay vertices
- Information whether electron is subject to bremsstrahlung
- PDG id and barcode of bremsstrahlung child electron if existent
- Energy and vertex information of bremsstrahlung photon if existent
- Information whether bremsstrahlung photon converts
- PDG id, barcode, vertex and energy information on conversion electrons if existent

With this additional information on the GEANT electrons it was possible to trace a generator level electron on its way through the detector and find all its bremsstrahlung products. As will be shown in the following chapters this reveals important information on electron charge misidentification.

4.3 N-Tuple Analysis in Root

An actual analysis of detector data is usually based on flat n-tuples, which are created from the AOD or even ESD data files. The software package used for this purpose is Root, an object-oriented data analysis framework [14]. Root is developed in C++ and also uses a C++ type language for its command line interface and as scripting language. There also exists a Python interface to the Root libraries, called PyRoot [16]. Programs for this analysis are both written as C++ and Python scripts. The typical steps of an analysis program in Root consist of the following parts:

1. Opening the file containing the n-tuple. When using C++ it is necessary to implement forward definitions of all variables to be read from the n-tuple.

[1] The Particle Data Group (PDG) publishes a Monte Carlo particle numbering scheme in [15], which is used to unambiguously specify the type of a particle during simulation. This identification number is called PDG id.

[2] There is a unique identifier assigned to every Monte Carlo object in a simulated event. This unique identifier is called barcode.

2. Looping over all events in the n-tuple and collecting statistical information. This is the place, where the actual analysis code is implemented.

3. Displaying histograms and summary statistics of the collected data.

When using the PyRoot Python wrapper for the C++ Root program libraries, point one above is greatly simplified, since no forward definitions for any of the variables to read from the n-tuple need to be defined before using them in the program. This allows more rapid code development, although there might be a small runtime penalty due to the additional layer of code around the actual native Root libraries.

5 Electron Charge Misidentification

5.1 Electron Reconstruction and Charge Identification

5.1.1 Ingredients to Electron Reconstruction

There are two main ingredients to electron reconstruction. One is the cluster in the electromagnetic calorimeter, the other is the track from the Inner Detector that is matched to this cluster.

Electromagnetic Calorimeter Cluster

A particle depositing energy into the electromagnetic calorimeter does this by creating an electromagnetic shower. Thus the energy of the particle will be spread out over some area within the calorimeter. The electromagnetic calorimeter is arranged in cells with certain dimensions in the ϕ and η directions as well as a given depth. The electromagnetic calorimeter consists of three layers of such cells (see chapter 3). An area into which a certain amount of energy is deposited is then considered a cluster. The calorimeter topology gives rise to a number of variables describing the shape of the shower within the calorimeter, which can be used to discriminate different types of particles.

In the case of electrons the energy of the electron is solely determined by the energy deposited in the electromagnetic calorimeter.

Track in the Inner Detector

While the cluster in the electromagnetic calorimeter in terms of reconstruction can be considered the actual electron, a track in the Inner Detector pointing to the calorimeter cluster gives important additional information about the electron. In ATLAS all electrons are required to have a matching track from the Inner Detector. Clusters in the electromagnetic calorimeter which have no track associated to them are reconstructed as photons, given the shower is of compatible shape. Therefore aside from the fact of its mere existence, which marks the cluster as an electron as opposed to a photon, the main information a track associated to a calorimeter cluster yields is the actual charge of the electron. Also a number of quality criteria foot on the comparison of track and cluster variables and the agreement of cluster and track, which is addressed in the following subsections 5.1.2 and 5.1.3, describing the workings of the electron reconstruction algorithms.

5.1.2 Track-Based Electron Reconstruction

A possible starting point for the reconstruction of an electron is a track in the Inner Detector. In ATLAS jargon electrons reconstructed this way are called *soft electrons*. This algorithm has been developed for electrons at low transverse momentum, p_T, and

for electrons in jets. However, this algorithm is also suitable for finding electrons at high transverse momenta [17].

The track-based electron reconstruction is seeded by a high quality track in the Inner Detector. The track is subject to the following requirements from the Pixel and SCT detectors[1]:

- The transverse momentum, p_T, of the track has to be greater than 2 GeV.
- The track needs to have at least nine precision hits, i.e. hits within the Pixel and SCT detectors. At maximum 25 precision hits are possible, 9 in the three layers of the Pixel detector and 16 in the four layers of the SCT tracker.
- At least two of these hits must have occurred in the Pixel detector, with at least one of them occurring in the first layer.
- The absolute value of the impact parameter of the track in the transverse plane[2], d_0, has to be less than 1 mm.

There are two additional requirements in order to reduce the amount of particles falsely reconstructed as electrons, called fake electrons, using information from the TRT detector [17].

- At least 20 hits in the TRT detector are required along the track. The maximum number of hits that can be generated in the TRT detector is 46.
- At least one of them also needs to be a high threshold hit.

These selection rules have two important consequences. One concerns the value of the `IsEM` flag, which is described below. All electrons reconstructed by this track-based algorithm will pass a cut on the `IsEM` value of `0x10f0000`. The other consequence is that the TRT requirement limits the pseudorapidity range of this reconstruction algorithm to values of $|\eta| < 2$.

All the tracks that fulfill the above criteria are then extrapolated to the electromagnetic calorimeter, where a cluster is created around the extrapolation point. Again some quality criteria involving cluster variables are applied:

- The ratio of the cluster energy and track momentum E/p needs to be greater than 0.7.
- The energy deposited in the first layer of the electromagnetic calorimeter, $E1$, needs to be greater than three percent of the total energy deposit, E, in all three layers: $E1/E > 0.03$
- More than half of the energy deposited in the electromagnetic calorimeter has to be accumulated in the first two layers: $E3/E < 0.5$

[1] For ATHENA release 14 only seven precision hits are required and the constraint on the transverse impact parameter d_0 is completely dropped.

[2] The impact parameter in the transverse plane is the distance of the point of closest approach of the (extrapolated) track of the electron to the beam axis.

These cuts help to reduce the chance of jets faking an electron. The number of electron candidates per jet is reduced from 9 to 0.4, while the electron reconstruction efficiency is reduced by about 10% [17].

5.1.3 Calorimeter Cluster-Seeded Electron Reconstruction

The other possible starting point for an electron reconstruction is a cluster in the electromagnetic calorimeter. To this end a Sliding-Window-Algorithm is used. It runs in three steps: tower building, pre-cluster (seed) finding and cluster filling [17].

The tower building step geometrically divides the $\eta - \phi$ space of the calorimeter into a grid of N_η by N_ϕ elements, each of size $\Delta\eta \times \Delta\phi$. For electromagnetic objects the calorimeter within the η range of ± 2.5 is divided into $N_\eta = 200$ by $N_\phi = 256$ elements, leading to a element size of $\Delta\eta = \Delta\phi = 0.025$. The energy inside these elements is summed across the layers of the calorimeter to give the tower energy [17].

A window of $N_\eta^{window} \times N_\phi^{window} = 5 \times 5$ in units of the tower size $\Delta\eta \times \Delta\phi$ is then slid across the grid defined above. If the sum of the transverse energy of the towers contained in this window is above a certain threshold value E_T^{thres} a pre-cluster at this point is formed. If there are multiple pre-clusters found that are in close proximity to each other, only the pre-cluster with the largest transverse energy is kept. The positions of the pre-clusters are then used as seeds around which final clusters are filled. The final electromagnetic clusters include all cells that are located inside a rectangle of size $N_\eta^{cluster} \times N_\phi^{cluster} = 5 \times 5$ centered on the seed position [17].

The clusters are then matched to tracks. The η and ϕ at the origin of the track are compared to η and ϕ of the cluster. If they are in agreement within 0.05 in η and 0.1 in ϕ, then in a second step the track is extrapolated to the cluster and is again compared in η and ϕ for each layer and the difference is required to be less than 0.025 and 0.05, respectively [17]. Thus the direction of the shower in the electromagnetic calorimeter needs to be in agreement with the direction of the track.

In contrast to the track-based algorithm, with the calorimeter based algorithm there are no general constraints on the track, which is matched to the cluster.

5.1.4 Important Variables in Electron Reconstruction

There are a number of variables that result from the reconstruction of electrons. Some of them have their origin solely in the calorimeter cluster others are pure track parameters and a third class is made of variables that combine track and calorimeter entities. Below a short non-exhaustive overview over important reconstruction variables is given. The names in brackets denote the standard name of the variable in the n-tuple.

Calorimeter Variables

Energy (`El_E`) This is the total energy of the electron candidate. It is exclusively calculated from calorimeter measurements. The cluster energy is corrected for modulations of the calorimeter response in η and ϕ and for any leakage outside the cluster, as well as other geometrical effects [17].

Energy in the Second Layer in 3×3 and 3×7 Cells (`El_e233` and `El_e237`) The electromagnetic calorimeter consists of three layers. The fraction of energy deposited in each layer of the calorimeter compared to the total amount of energy deposited in the calorimeter can give some indications about what type of particle was responsible for the deposit. In the case of electrons, this information on shower depth is considered for the calculation of the electron quality criteria `El_IsEM`.

The two variables `El_e233` and `El_e237` contain the amount of energy deposited in the second layer of the electromagnetic calorimeter in 3×3 and 3×7 sized $\eta \times \phi$-calorimeter cells respectively around the center of the cluster. The ratio of the two gives information on the lateral shower shape and will be later used to attempt to identify electrons that suffer heavily from bremsstrahlung.

Transverse Energy in a Cone around the Electron Cluster (`El_etcone20`) This variable contains the energy deposit in the electromagnetic and hadronic calorimeters within a cone of $\Delta R = 0.2$ around the electron cluster, not including the energy of the electron cluster itself. This is a measure of the isolation of the electron. This variable is often used to distinguish isolated electrons from jets, which would show a higher amount of energy deposited in the vicinity of the electron cluster.

Difference between Cluster Phi and Track Phi (`El_deltaPhi2`) This variable describes the difference between the ϕ position of the center of the electromagnetic cluster in the second layer of the calorimeter and the ϕ value as a result from the extrapolation of the track associated to the cluster.

Track Variables

Eta (`El_eta`) and Phi (`El_phi`) Although the detector η and ϕ could also be calculated from the calorimeter cluster position, since in ATLAS all electrons are required to have a track, the η of the electron is calculated from the track associated to the electron cluster.

Transverse Impact Parameter (`Trk_d0`) The transverse impact parameter describes the distance at the point of closest approach between the beam or z-axis and the extrapolation of a reconstructed track. This variable is not part of the collection of electron variables in the AOD but can only be found in the collection of track variables in the AOD.

Combined Variables

Transverse Momentum (`El_p_T`) The transverse momentum of the electron is calculated from the total energy and the η of the electron. Since electrons are ultra-relativistic particles ($\beta \approx 1$) at the energies involved at LHC, their energy approximately is equal to the magnitude of the three-momentum of the electron, $E \approx |\mathbf{p}|$. Thus $p_T = \sin\left[2 \arctan\left(\exp(-\eta)\right)\right] \cdot E$

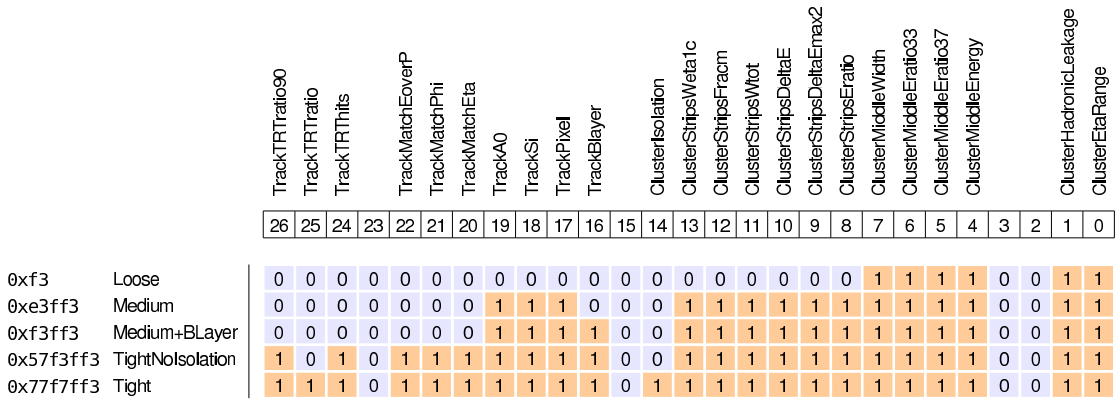

Figure 5.1: Bit flags within the `El_IsEM` reconstruction variable. Several standard bitmasks are indicated, such as for loose, medium or tight electrons. The hexadecimal number on the left is the bitmask value.

Ratio of Cluster Energy and Track Momentum (`El_EoverP`) Every reconstructed electron candidate consists of a calorimeter cluster and an associated track. The ratio E/p compares the cluster energy to the track momentum. In the ultra-relativistic case, this ratio would ideally be unity. Higher values of E/p hint towards bremsstrahlung losses of the electron in question.

Other Variables

Electron Author (`El_author`) The variable called `El_author` specifies which algorithm was used reconstructing this electron candidate. It has three possible values. In the case of the calorimeter-based algorithm it contains the value 1 and in the case a track-based reconstruction was used it holds the value 2. If this electron candidate was reconstructed by both algorithms the value of `El_author` is 3.

IsEM Bitmask (`El_IsEM`) The `El_IsEM` bitmask contains information on whether this electron candidate has passed certain quality cuts. This variable will be described in detail in the following subsection.

5.1.5 Quality Criteria for Reconstructed Electron Candidates

The electron objects reconstructed with either algorithm described in subsections 5.1.2 and 5.1.3 are electron candidates in the sense that there is still a chance that they are caused by another object than an electron, such as a jet or a charged pion. Accepting losses in the electron reconstruction efficiency one can apply certain cuts and methods in order to reduce such fake electrons. The most common way to characterize an electron candidate is the *IsEM* variable. This variable consists of 26 bits and contains the results to certain cuts that where applied after reconstruction. When such a cut fails, a bit at a specified position within IsEM is set and can be tested during analysis. Figure 5.1 shows the bits within the `El_IsEM` variable.

In ATLAS there are three main standard categories for electron candidates. These are *loose*, *medium* and *tight*. Figure 5.1 also specifies what cuts are necessary to be passed by an electron candidate in order to fit in any of these categories. The hexadecimal number on the left side is the bitmask value against which the `El_IsEM` variable needs to be tested. For instance all loose electron objects fulfill the condition `El_IsEM` & `0xf3` = 0, where the '&' denotes a bitwise-and operation, since any of the cuts corresponding to the bits 0, 1 and 4 through 7 must not have failed.

Below there is a short overview over the most important entries in the IsEM flag. Bits 0 through 14 correspond to cuts on calorimeter variables only. Bits 16 through 19 correspond to cuts on tracking variables only, while bits 20 through 22 are concerned with cuts that involve both tracking and calorimeter variables. Information from the TRT tracker is taken into account for bits 24 through 26.

Bit 1: ClusterHadronicLeakage For electrons most of their energy will be deposited in the electromagnetic calorimeter, while jets and charged pions will leave a considerable deposit in the hadronic calorimeter as well. This bit indicates whether the energy in the first layer of the hadronic calorimeter is greater than a certain fraction of the energy deposited in the electromagnetic calorimeter.

Bit 16: TrackBLayer This bit indicates whether the track associated to the electron candidate has a hit in the first layer of the Pixel tracking detector.

Bits 17 and 18: TrackPixel and TrackSi These bits indicate whether the track has a certain amount of hits in the Pixel and SCT detectors. If both bits are set, a total of nine precision hits, i.e. hits in either of the two detectors is required, where at least two of these hits are required to have occurred in the Pixel detector. Typically an electron generates around 3 hits in the Pixel detector

Bit 19: TrackA0 This bit is concerned with the transverse impact parameter. If this bit is set the distance of the point of closest approach to the beam axis, d_0, was greater than 1 mm.

Bit 22: TrackMatchEoverP The energy of the electron as in `El_E` is compared to the momentum of the track that is associated to the electron cluster. It is favorable that these numbers are in agreement. This bit is set when the electron candidate fails to have an acceptable value for $E_{\text{electron}}/p_{\text{track}}$ between 0.7 and 4.0.

5.1.6 Determination of the Charge of the Electron

The information gained from the calorimeter might give enough information to securely identify an object as an electron or a photon. The existence of a track that can be associated to the cluster in the electromagnetic calorimeter then makes it possible to distinguish between electrons and photons. Moreover the tracking information can improve the identification of electrons even further as it is done in combined variables such as E/p or requiring a certain number of precision hits.

In order to identify the charge of an electron the curvature of its associated track in the magnetic field of the Inner Detector is the only way to accomplish this goal. The curvature of a track as the inverse of its radius is given by

$$C = \frac{1}{R} = B_z \frac{q}{p_T}\,, \tag{5.1}$$

where B_z is the magnetic field strength in the direction of the beam axis and $q \in \{-1, 1\}$ the charge of the electron. At high values of p_T the curvature can become rather small. Any scattering processes within the detector that cause a 'kink' or a small deflection of the track of the electron can lead to a wrong measurement of the sign of C and thus to a charge misidentification. Granularity and resolution of the detector will also be of importance. It will be shown however in chapter 6 that these are not the dominating effects leading to charge misidentification unless in the case of very high transverse momentum of more than several hundred GeV.

5.2 The Issue of Charge Misidentification

5.2.1 Electron Charge Misidentification in Simulated Data

Detector Simulation takes place in three steps. First the actual physics event is simulated. Particles created in this step are called to be *on generator level*. Next these generator level particles are the input for the detector simulation where their interaction with the detector material and the full detector response is simulated. The output of detector Monte Carlo simulation data, i.e. the simulated detector response is then fed into particle reconstruction as if it were actual data. The definition of electron charge misidentification in this scenario is then straightforward:

Definition 5.1 (Electron charge misidentification in Monte Carlo Data)**.** If the charge of the generator level electron is different from the charge of the corresponding reconstructed electron, the reconstructed electron is said to be charge misidentified.

The above definition raises one important question however, namely how the correspondence between the generator level electron and the reconstructed object is established. This process is called matching.

5.2.2 Matching Monte Carlo Electrons to Reconstructed Electrons

A simple but effective method was applied for matching Monte Carlo truth electrons to their reconstructed counterparts. The distance ΔR between two points in the η-ϕ plane is defined by

$$\Delta R = \sqrt{\Delta\eta^2 + \Delta\phi^2}\,. \tag{5.2}$$

Monte Carlo and reconstruction objects are said to be related when they are within a certain distance to each other. The cutoff value for ΔR did not show to be critical in the datasets used for this analysis. A common choice for the value of ΔR is 0.1. This turned out to be a sensible value. The matching efficiency, i.e. the fraction of

reconstructed electrons for which it was possible to find a matching Monte Carlo electron is close to one for all datasets used and on the other hand with this value there were few matching ambiguities, i.e. cases where more than one possible Monte Carlo match for a reconstructed electron was found.

5.2.3 Electron Charge Misidentification in Actual Data

Definition 5.1 above, that was given for the case of Monte Carlo simulation, can be taken to the case of actual data with only little modification.

Definition 5.2 (Electron charge misidentification)**.** If the charge of an electron entering the detector is different from the charge of the corresponding reconstructed electron, the reconstructed electron is said to be charge misidentified.

The only difference to the first definition lies in the fact that the latter case is not directly testable, since obviously one does not know the charge of the electron entering the detector.

5.3 Electron Charge Misidentification in Z→ee, ttbar and Single Electron Datasets

5.3.1 The Datasets

In this section three types of datasets will be looked at. These are

- single electron samples at different values for p_T,
- a $t\bar{t} \rightarrow$ lepton+jets, dilepton sample and
- a $Z^0 \rightarrow e^+e^-$ sample.

The datasets are all reconstructed using ATHENA release 13. In contrast to the single electron samples, the latter two are full physics samples, which means that complete the proton-proton collision is fully simulated. In addition to the named physics process there are therefore additional objects in the sample that stem from the collision event.

Table 5.1 shows an overview of the magnitude of the charge misidentification probabilities in the different samples. The error given is a statistical 1σ binomial proportion confidence interval. The misidentification rate is an average over the entire η range and over all p_T values. From the single electron samples at different p_T values it can be seen that the charge misidentification rate does increase considerably with increasing transverse momentum. This will be looked at in greater detail in subsection 5.3.3.

Another thing to note is that the electron reconstruction efficiency is degraded in the $t\bar{t}$ sample. The reconstruction efficiency is defined as the number of reconstructed electrons with a given IsEM flag value divided by the number of Monte Carlo truth electrons within the reconstruction η range ($|\eta| \leq 2.5$). The $t\bar{t}$ dataset includes the lepton+jets decay channel in addition to the dilepton channel. The relative contribution of the l+jets decay channel is about four times the contribution of the dilepton channel [15]. This means there is high hadronic activity and such there are a number of electrons within jets

that are not as efficiently reconstructed by the algorithm, which works best for isolated electrons. The numbers for the reconstruction efficiency for the $Z \rightarrow ee$ sample appear plausible, comparing them to the numbers for a single electron dataset.

5.3.2 Eta dependence of Charge Misidentification Probability

The numbers for the electron charge misidentification rate in table 5.1 are averaged over the entire η range from -2.5 up to 2.5. The rate of electron charge misidentification however depends strongly on the pseudorapidity of the electrons. Figure 5.2 shows the charge misidentification probability versus the pseudorapidity η for medium electrons in the $Z \rightarrow ee$ sample. While in the center region within $|\eta| < 1$ the misidentification rate is below 10^{-3} it rises steeply with increasing magnitude of η to values greater than one percent for $|\eta| > 2$. Neither is the p_T distribution of the electrons grossly affected by the choice of η, nor is there any reason why the detector resolution should be degraded to this extent for higher η compared to the center region. Most Z^0 bosons are produced with low transverse momentum and therefore kinematics restrict the p_T range within the $Z \rightarrow ee$ sample to values usually below half the mass of the Z^0 boson, m_Z, and thus should easily be manageable by the ATLAS detector. The p_T distribution of the reconstructed medium electrons in the $Z \rightarrow ee$ sample is shown in figure 5.3. The increase of the charge misidentification rate with η then has to have other sources. Looking at figure 5.4, which shows the material budget of the Inner Detector in units of radiation lengths, a close resemblance is seen. Electrons passing through the detector material naturally do

Table 5.1: Overview of the magnitude of charge misidentification probabilities in different samples. The error shown is a statistical 1σ binomial proportion confidence interval. The misidentification rate is integrated over the entire η and p_T ranges. The reconstruction efficiency is also shown. This efficiency is the ratio of the number of reconstructed electrons and the number of Monte Carlo electrons within the reconstruction η range ($|\eta| \leq 2.5$).

Sample	IsEM	Efficiency	Misid. Rate
Single e (60 GeV)	Medium (`0xe3ff3`)	83.2%	$(6.46 \pm 0.45) \cdot 10^{-3}$
	Tight (`0x77f7ff3`)	68.2%	$(4.40 \pm 0.41) \cdot 10^{-3}$
Single e (120 GeV)	Medium	84.9%	$(1.15 \pm 0.05) \cdot 10^{-2}$
	Tight	71.6%	$(8.25 \pm 0.48) \cdot 10^{-3}$
Single e (1000 GeV)	Medium	90.0%	$(7.55 \pm 0.12) \cdot 10^{-2}$
	Tight	61.8%	$(4.60 \pm 0.12) \cdot 10^{-2}$
$t\bar{t} \rightarrow$ non all hadronic	Medium	68.1%	$(4.72 \pm 0.17) \cdot 10^{-3}$
	Tight	52.5%	$(2.30 \pm 0.13) \cdot 10^{-3}$
$Z \rightarrow ee$	Medium	76.6%	$(4.38 \pm 0.10) \cdot 10^{-3}$
	Tight	59.9%	$(2.41 \pm 0.09) \cdot 10^{-3}$

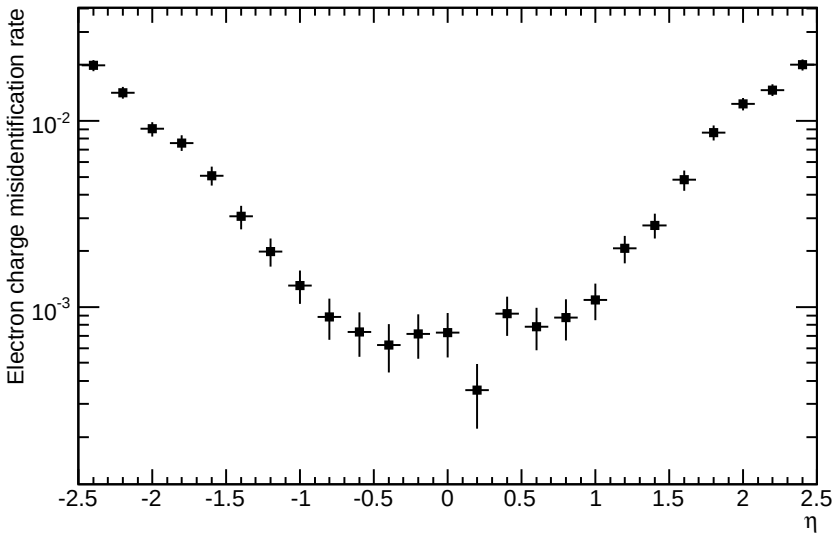

Figure 5.2: Electron charge misidentification rate for medium (IsEM & `0xe3ff3` = 0) electrons in $Z \to ee$ vs. pseudorapidity η.

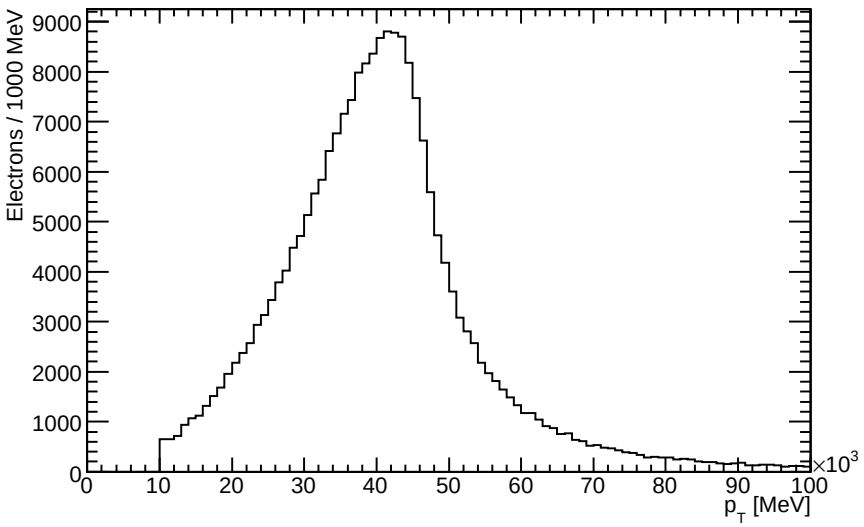

Figure 5.3: Distribution of the reconstructed transverse momentum p_T of medium electrons in the $Z \to ee$ sample ($p_T > 10\,\text{GeV}$). The total number of reconstructed medium electrons is 405241 in 346000 events. Only electrons within $|\eta| < 2.5$ can be reconstructed.

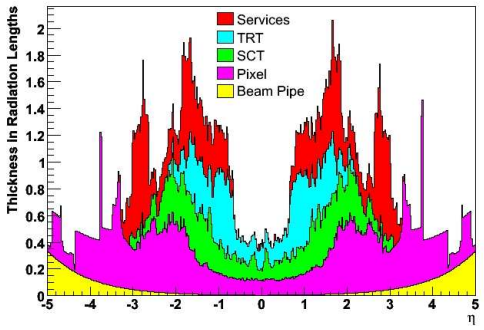

Figure 5.4: Material budget of the Inner Detector in radiation lengths vs. η [18].

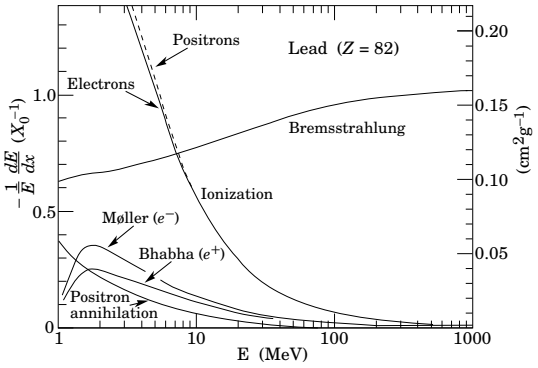

Figure 5.5: Fractional energy loss per radiation length in lead as a function of electron energy [15].

not only interact with the electromagnetic calorimeter but also with elements of the tracking detector. Therefore it seems likely that electron charge misidentification is caused by an interaction of the electron with the detector material. Figure 5.5 taken from [15] shows the fractional energy loss per radiation length in lead as a function of the electron energy. For electron energies above several hundred MeV almost all energy loss is due to bremsstrahlung and scattering or ionization effects play only a minor role. Bremsstrahlung in matter can of course lead to deflections and kinks in the track of the electron and such result in a wrong measurement of the sign of the curvature of the track. Also, there is the possibility of subsequent conversion of the bremsstrahlung photon also having the ability to confuse the reconstruction algorithms. Charge misidentification due to bremsstrahlung and subsequent conversion will be discussed in detail in the next chapter.

5.3.3 Dependence of Charge Misidentification Probability on Transverse Momentum

Earlier in equation 5.1 an expression for the curvature of a track in the transverse plane was given. Increasing the value of p_T in the denominator leads to smaller values for C. At higher transverse momentum an erroneous measurement of the curvature thus will more likely lead to a wrong determination of the sign of C.

Figure 5.6 shows the charge misidentification probability versus the transverse momentum in the $Z \rightarrow ee$ sample. Clearly the misidentification rate rises with increasing p_T. At the high end however statistics is very low since the p_T range in the $Z \rightarrow ee$ dataset is limited by the kinematics of the Z^0 decay.

5.3.4 Electron Author and Charge Misidentification Rate

In subsection 5.1.4 the `El_author` variable was introduced that indicates which reconstruction algorithm was responsible for the reconstruction of the electron candidate. As can be seen from figures 5.7 and 5.8 the charge misidentification probability depends

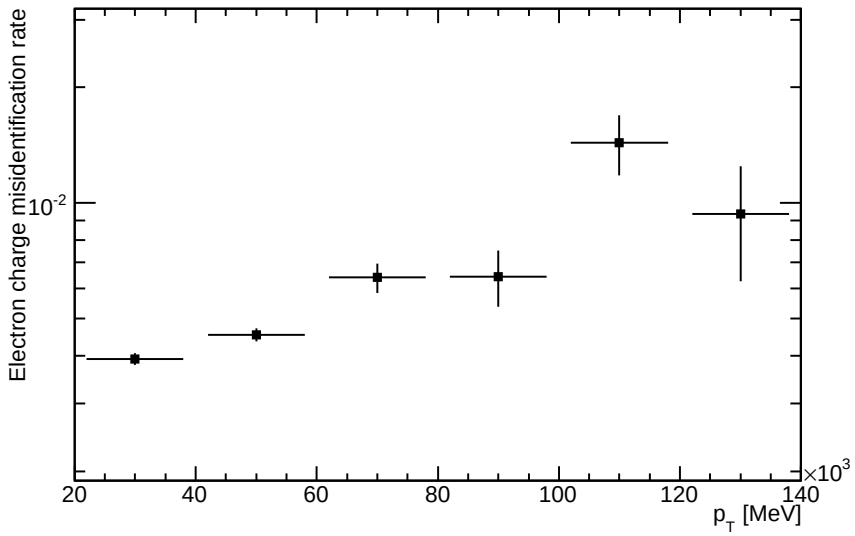

Figure 5.6: Electron charge misidentification rate versus transverse momentum p_T as seen in the $Z \rightarrow ee$ sample.

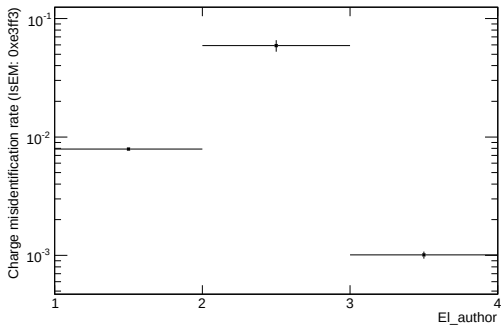

Figure 5.7: Electron charge misidentification rates for different authors. Electrons were required to pass medium quality cuts.

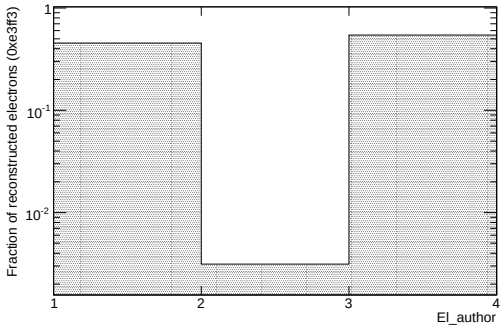

Figure 5.8: Fraction of electrons reconstructed by a certain author. Electrons were required to pass medium quality cuts.

on the reconstruction algorithm. About half of the electrons are reconstructed by the calorimeter-seeded algorithm only (`El_author`=1), while the other half of electron candidates is found by the calorimeter as well as the track-based algorithm (`El_author`=3). There is also a small number of electrons that were found by the track-based algorithm only (`El_author`=2). Electrons with an `El_author` value of 3 have a charge misidentification probability of less than half than electrons reconstructed by only the calorimeter-based algorithm. Electrons found by only the track-based reconstruction have a relatively high chance of being charge misidentified. They however make up for only less than 5 percent of the medium electrons in the $Z \rightarrow ee$ sample.

6 Charge Misidentification through Bremsstrahlung and Conversion

6.1 Bremsstrahlung and Conversions in Monte Carlo

6.1.1 Bremsstrahlung and Charge Misidentification

In the previous chapter the assumption was made that bremsstrahlung and conversion of electrons in the detector material might be of importance to the issue of electron charge misidentification. Supporting this statement is the fact that bremsstrahlung and conversion are much more prevalent when looking only at misidentified electrons than it is when looking at all electrons in a dataset. This is shown in figure 6.1. The plot shows a histogram for misidentified electrons and all reconstructed electrons. The number that is plotted in the histogram denotes the number of bremsstrahlung photons produced within the Pixel and SCT detectors that *one* generator level electron is responsible for, i.e. that generator level electron is the common parent to all the bremsstrahlung photons. The plot clearly shows that the distribution of the number of bremsstrahlung photons coming from one generator level electron is shifted to higher values for the electrons which are charge misidentified. On average an electron leads to 1.6 bremsstrahlung photons, while a misidentified electron is on average responsible for 2.7 bremsstrahlung photons. It was shown in figure 5.2 that the misidentification probability rises with increasing η. The same is obviously true for the number of bremsstrahlung photons coming from a generator electron, since in the case of a greater η value more detector material is there to be crossed by the particle. In order to avoid seeing an increased number of bremsstrahlung photons only due to the fact that charge misidentification is more likely at higher η values, where also bremsstrahlung is also more likely to happen due to more detector material in the path of the electron, only generator level electrons in the η range of ± 1.5 are considered for the histogram. Figure 6.2 shows the other side of the same coin, namely the number of *conversions* of bremsstrahlung photons within the Pixel and SCT detectors, having the same generator level electron as a common parent. It seems obvious that in the case of charge misidentified electron where there are a greater number of bremsstrahlung photons to start with, there is also a higher number of conversions. The numbers are however quite striking. Whereas only about 20% of all generator level electrons within $|\eta| < 1.5$ lead to at least one pair of conversion electrons, more than 90% of the misidentified electrons give rise to at least one pair and still more than 20% of them are a parent for two converted bremsstrahlung photons.

6.1.2 Reconstruction Track Multiplicity

In subsection 6.1.1 it was described that for charge misidentified electrons one finds a higher number of bremsstrahlung photons and conversions in Monte Carlo information than it is the case for all electrons. This effect can also be seen in reconstruction. The

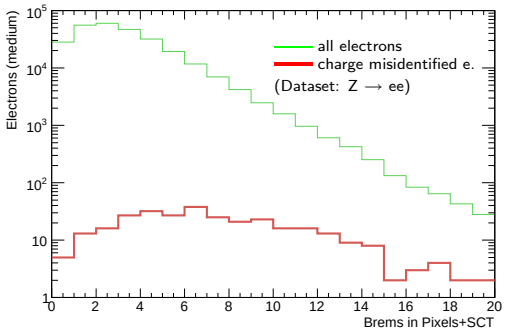

Figure 6.1: Number of bremsstrahlung photons generated within the Pixel and SCT trackers from generator level electrons with $|\eta| \leq 1.5$.

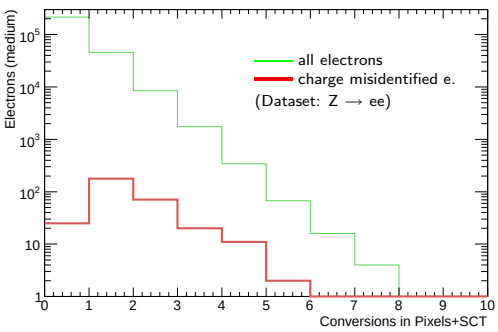

Figure 6.2: Number of conversions of bremsstrahlung photons within the Pixel and SCT trackers from generator level electrons with $|\eta| \leq 1.5$.

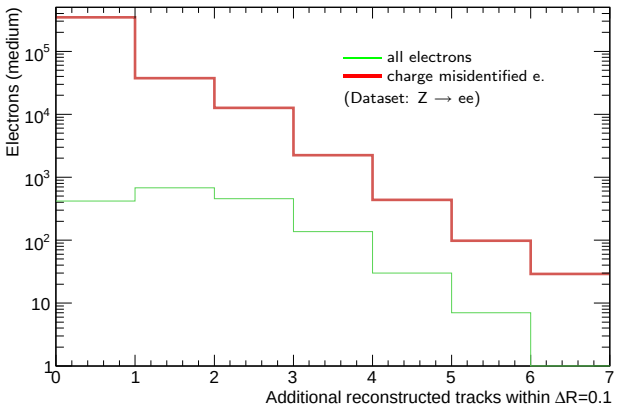

Figure 6.3: Number of close tracks within a distance of $\Delta R \leq 0.1$ around the track of the electron for all reconstructed electrons and charge misidentified electrons.

conversion electrons will also lead to hits within the Inner Detector and if the conversion happens early enough and a sufficient amount of energy is transferred to the conversion electron, a track will be reconstructed from the hits. In general the conversion electrons and bremsstrahlung photons will contribute to the cluster energy of the electron in question and will not lead to isolated clusters. Thus the additional reconstructed tracks will not lead to another electron candidate, but they are accessible as separate tracks in the track collection of the reconstruction data files.

Figure 6.3 shows the number of tracks found within a distance $\Delta R \leq 0.1$ around the track of the electron for all electrons and for charge misidentified electrons. For almost 90% of all electrons no additional track close to the track of the electron can be found. However, in more than 80% of the cases for misidentified electrons there is at least one additional track near the track belonging to the reconstructed electron object.

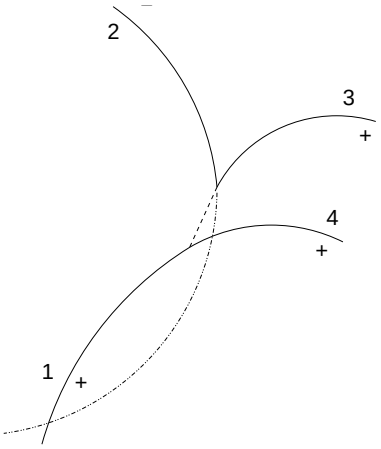

Figure 6.4: Simple model and naming scheme for bremsstrahlung and conversion events.

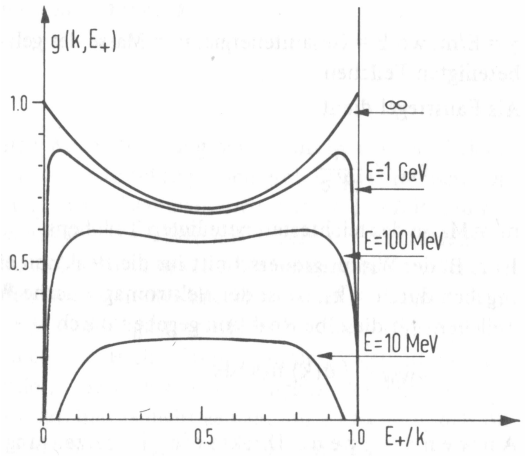

Figure 6.5: Odds for a conversion electron getting a certain energy fraction of the photon energy for different photon energies [19].

6.1.3 A Simple Model for Electron Charge Misidentification

A simple model and naming scheme for electron charge misidentification through bremsstrahlung and conversion will be introduced in this subsection. Figure 6.4 depicts the situation of a bremsstrahlung with subsequent conversion. For illustration purposes the diagram is not drawn to scale. Solid lines are the actual tracks of the electrons involved. The numbering provides a way of referencing the tracks while the + and - symbols denote the *relative* charge of the electrons with respect to the initial electron '1'. Walking through the model starting at the lower left corner electron '1' with charge '+' is on its way through the detector. At some point Bremsstrahlung through interaction with the material in the detector occurs. A bremsstrahlung photon is emitted, denoted by the dashed line. A portion of the energy of electron '1' is transferred to the photon, the rest of the energy remains with the electron, which will continue on a track with higher curvature due to its lower energy and now is denoted with '4'. In Monte Carlo data, the electrons '1' and '4' are treated as two different particles related only by a parent-child relationship. In case the bremsstrahlung photon converts through interaction with the detector material it will produce a pair of electrons, '2' and '3'. Since the photon carries no charge, the sum of the charges of the two conversion electrons must be zero. Thus one of the two electrons, denoted with '3' will be curved in the same direction as electrons '1' and '4', while electron '2' with the opposite charge to '3' will be curved the other way in the magnetic field of the Inner Detector.

Figure 6.4 shows a possible reason for the higher number of tracks seen in the case of charge misidentified electrons. Each electron denoted '1' through '4' is possibly the source of a reconstructed track. How this can lead to charge misidentification is indicated by the dash-dotted line, which is the extrapolation of the track of electron '2'. Suppose that electron '1' is the generator level electron, whose charge one is interested in. It could give a considerable fraction of its energy to the photon in the event of bremsstrahlung in the

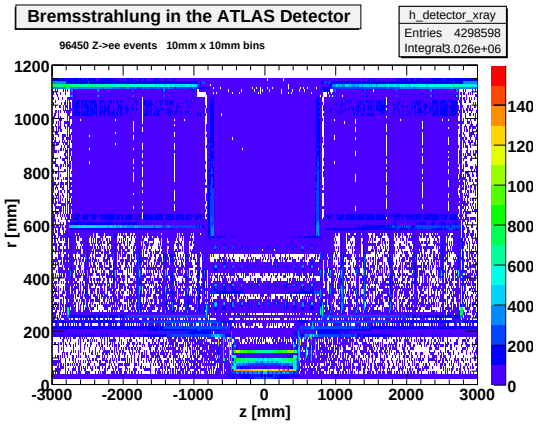

Figure 6.6: ATLAS detector "x-ray". Bremsstrahlung photon production vertices in the z-R plane. Each point in the diagram color codes the number of bremsstrahlung photons produced on a ring with radius r around the beam axis at the position z from the center point.

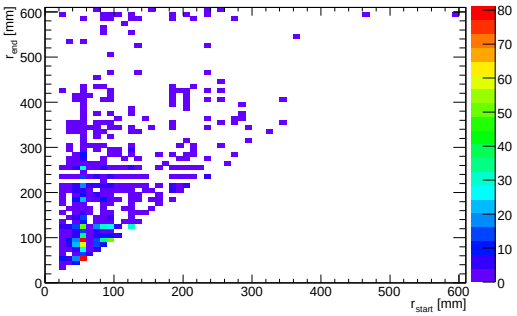

Figure 6.7: Start versus end distances of the bremsstrahlung photon with highest energy in a shower. This plot shows the distance of bremsstrahlung photons from the beam axis at their creation and conversion.

detector material. After conversion, electron '2' might end up with a comparable energy to the energy that electron '1' started out with. If this process happens early enough in the detector it is even possible for such an electron to pass tight quality criteria for reconstructed electrons. The track finding algorithm might even consider hits, originally coming from electron '1', to fit the track of electron '2', as indicated by the intersection of the solid line of electron '1' and the dash-dotted line. At energies involved in the LHC and ATLAS it is indeed quite likely that one of the two conversion electrons receives a considerable fraction of the energy of the bremsstrahlung photon. Figure 6.5 shows the odds for a conversion electron to receive a certain energy fraction E_+/k of the total photon energy $E = k$ during conversion. For higher photon energies the probability for one electron to receive almost all the energy of the photon is increasing.

6.1.4 Where does Bremsstrahlung and Conversion Occur

For the matter of electron and track reconstruction, it is an important question where bremsstrahlung and conversion do occur. In ATHENA release 13, a reconstructed track must start before the TRT sub-detector, while in ATHENA release 14 reconstructed tracks are allowed to exclusively consist of TRT hits. These tracks however will not pass quality criteria for medium or tight electrons. Therefore this change is not of great concern for this study. Medium electrons are required to have a certain number of precision hits, i.e. hits in the Pixel or SCT tracking detectors. In the previous subsection 6.1.3 it was suggested that a conversion electron, if it appears early enough in the detector, might lead to electron charge misidentification. This raises the question where bremsstrahlung predominantly occurs in the ATLAS detector. Figure 6.6 shows

the vertices of bremsstrahlung photons being produced in the ATLAS detector in the $Z \rightarrow ee$ sample. The color coded histogram shows for each point in the z-R plane the total number of bremsstrahlung photons produced in a ring with radius r at z around the beam axis. Apart from some non-active material belonging to support structures for the Transition Radiation Tracker at high r values, the most active region in terms of bremsstrahlung photon production is the Pixel detector, especially the first layer. Bremsstrahlung photons are however not the only ingredient to the misidentification mechanism described in the subsection above. The bremsstrahlung photons also have to convert within the detector material.

Figure 6.7 shows the distance from the beam axis of the bremsstrahlung photon with the highest energy in the bremsstrahlung-conversion cascade (shower) at its creation, i.e. when bremsstrahlung occurs, and at the conversion of this photon into two electrons. Clearly one can see the position of the first layer of the Pixel detector, the b-layer, as a vertical line of high number entries in the histogram at a position of $r_{start} \approx 50\,\text{mm}$ (compare with figure 3.2). In most of the cases of charge misidentified electrons the highest energetic bremsstrahlung photons are created in the first layer of the Pixel detector and do also convert in this layer or the second layer. There is also a considerable number of bremsstrahlung photons coming from the first layer that are converted in the third layer. The situation for bremsstrahlung photons generated in the second layer at around $r_{start} \approx 90\,\text{mm}$ is quite similar. Most of the bremsstrahlung photons coming out of this layer are converted within the same layer or the third layer of the Pixel detector. Again, this would be sufficient to pass the quality criteria for medium electrons.

6.1.5 Relative Charge of Close Tracks

With figure 6.4 in subsection 6.1.3, a simple model for electron charge misidentification through bremsstrahlung and subsequent conversion was introduced. The two conversion electrons carry opposite charges. It was also shown that for charge misidentified electrons a higher number of nearby tracks is found than it is the case for all electrons. Also in subsection 6.1.3 it was suggested that electron charge misidentification comes from associating the track of the oppositely charged conversion electron with the calorimeter cluster of the reconstructed electron candidate. Assuming that the additional nearby tracks seen are the reconstructed remnants of the bremsstrahlung and conversion process a statement about the charges of these tracks can be made.

Events with One Nearby Track In the case of a correctly identified electron with one additional track (within a distance of $\Delta R \leq 0.1$), assuming the nearby track stemming from either of the two conversion electrons (denoted by '2' and '3' in the model), the relative charge of this track compared to the charge of the track belonging to the electron is either +1 or -1. Since there is no reason why either one of the two conversion electrons should be preferred, an even distribution of the two cases is expected when looking at a collection of such events.

On the other hand for misidentified electrons it is expected that the majority of the nearby tracks have a negative relative charge compared to the charge of the track of the electron, since it is the track of conversion electron '2' that is supposedly associated to

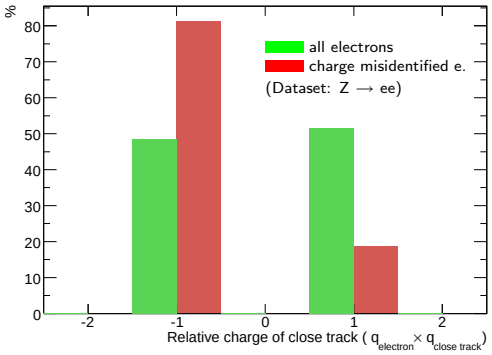

Figure 6.8: Relative charge of nearby track for events with exactly one additional close reconstructed track within $\Delta R \leq 0.1$ (medium electrons).

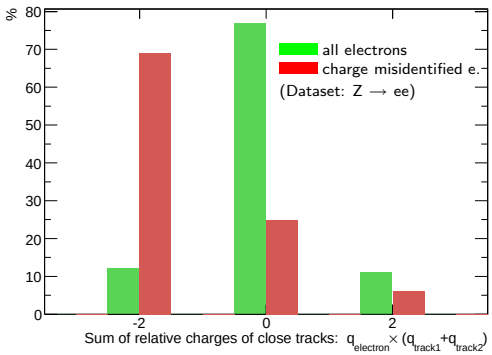

Figure 6.9: Sum of relative charges of nearby tracks for events with exactly two additional close reconstructed tracks within $\Delta R \leq 0.1$ (medium electrons).

the electron candidate and thus there are only oppositely charged particles (electrons '3' and '1'/'4') left to generate the additional track. The actual distribution as it was found in the $Z \rightarrow ee$ sample is shown in figure 6.8. More than 80% of events with one additional track in the case of charge misidentification show the assumed behavior. For all electrons, the relative charge of the close track is evenly distributed between the two possible values, as it was suggested by this model.

In about 20% of the cases of charge misidentified electrons the nearby track shows the same charge as the track of the electron candidate. An important assumption that has not been mentioned so far is, that all tracks are coming from the same bremsstrahlung and conversion process. This does not have to be the case. It is very well conceivable that more than one conversion contributes to the set of reconstructed tracks. In this scenario the charges of the tracks are not correlated anymore and thus are expected to distribute evenly over the two bins.

Events with Two Nearby Tracks What was said about events with one additional track can be extended to events with two tracks. Again tracks within a distance of $\Delta R \leq 0.1$ around the track of the electron are considered. In the case of correctly charge identified electrons, the sum of the relative charges of the two additional tracks is then expected to be zero, while for charge misidentified electrons the sum of the relative charges is expected to be -2. Figure 6.9 depicts the situation found in the $Z \rightarrow ee$ sample. In about 70% of the cases for misidentified electrons, the relative charges of the two additional tracks sum up to the expected value of -2, while in more than 75% of the cases for all electrons the expected value of 0 is assumed. Again the assumption that all three tracks for the event come from the same bremsstrahlung and conversion process is necessary to make any statements about the correlation of the track charges. If one or both tracks have a different source than the same bremsstrahlung and conversion process, then no statement about the respective charges can be made.

All in all the numbers do show a good support for the suggested simple model for electron charge misidentification.

6.2 The Simple Model for Electron Charge Misidentification revisited

While the previous section 6.1 pointed out the relation between bremsstrahlung and the topic of electron charge misidentification, introducing a simple model and some circumstantial evidence, this section will try to substantiate the assumption by directly relating Monte Carlo simulation truth information about electrons from converted bremsstrahlung photons to the reconstructed track of the misidentified electron.

The subsection about the E over p reconstruction variable will motivate the need for a revised concept of the relationship between reconstructed track and electromagnetic cluster in the case of charge misidentified electrons. This is followed by a study on the association of electrons from converted bremsstrahlung photons and the reconstructed tracks in the event of a charge misidentified electron. The findings on the transverse impact parameter will provide some further evidence to back the assumptions made.

The last subsection on charge misidentification in the regime of very high transverse momenta will show that the concept of charge misidentification through bremsstrahlung and conversion is the source for charge misidentification for transverse momenta up to some hundred GeV, but is dominated by other sources of charge misidentification for electrons at even higher transverse momenta.

6.2.1 E over p – Calorimeter Energy versus Track Momentum

A standard quality cut for electrons is the E over p cut, which compares the energy of the electron cluster to the momentum of the track that is associated to that cluster, together forming the electron candidate. In a perfect world the momentum of the track and the energy reconstructed in the calorimeter would the same, since electrons at the energies involved at ATLAS are ultra-relativistic particles and thus the relativistic energy-momentum relation simplifies to $E \approx p$. As was shown however, electrons suffer energy losses by interacting with the detector material mainly through bremsstrahlung. In that case the electron loses energy and photons with that energy are created. The bremsstrahlung photons created from high energy electrons have, within a narrow margin, the same direction as the electron [20]. At high transverse momenta, as they are found at the LHC, the electron and most of the bremsstrahlung photons will contribute to the energy of the same cluster. This means that the energy measurement of the cluster is a good reference for the energy of the original, say generator level, electron. The situation with the tracks is somewhat different. Energy losses of the electron will be reflected in a higher curvature of the fitted track. A comparison between the electron cluster energy from the electromagnetic calorimeter and the value of the transverse momentum from the track fitting algorithm will thus be a measure of how much an electron candidate suffered from bremsstrahlung on its way through the detector. If the discrepancy is too high the electron candidate is usually rejected, as it does not contain reliable information on the original object anymore. To this end the ratio of the calorimeter cluster energy and the track momentum, E/p is formed, and is referred to as E over p. The quality criteria for tight electrons as in the `El_IsEM` flag contain a cut on this value. There it

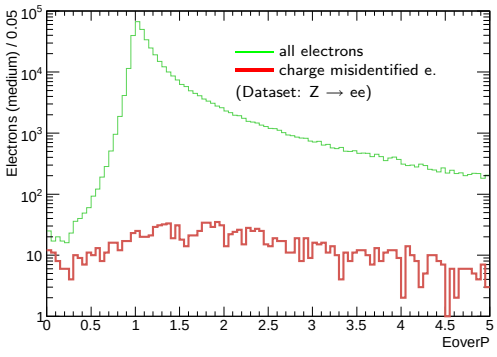

Figure 6.10: E/p for all reconstructed medium electrons and for charge misidentified electrons.

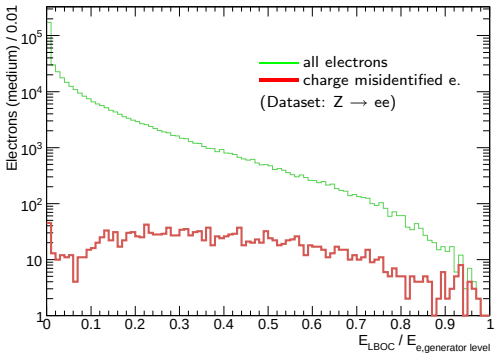

Figure 6.11: Fraction of generator level energy taken by the highest energetic conversion electron with a charge opposite to the generator electron. (LBOC)

is required that tight electrons must have an E/p value between 0.7 and 4. This means that electrons whose track momentum is below the calorimeter cluster energy by a factor of up to 4 can still be considered to be very good electron objects. In other words: about three quarters of the electron energy may be lost through bremsstrahlung.

As we have seen bremsstrahlung plays an important role in electron charge misidentification, so one expects that this fact is somehow reflected in the value of the E/p variable. In figure 6.10 this effect can clearly be seen. While in the case of all electrons the E/p distribution is sharply peaked at 1 with a steep rise and somewhat longer tail, which is caused by bremsstrahlung, the distribution for the charge misidentified electrons is flattened out. This is another strong indication that charge misidentification and bremsstrahlung are two closely linked subjects. While the application of an E/p cut for values below 0.7 and above 4 does cut away some of the misidentified electrons, the majority of them still remains within that range.

The confidence in the calorimeter cluster energy measurement is relatively strong due to the reasons mentioned before: the cluster collects energies within a certain spatial range and thus bremsstrahlung photons are likely to contribute to the energy of the electron. Also, the situation for conversion electrons is not too different. Either the conversion electrons carry only a tiny energy fraction compared to the original energy, then their paths are probably too curved to contribute to the cluster, but since their energies were low to begin with the cluster energy is affected only slightly. High energy conversion electrons will however contribute to the same cluster. The suspicion then is that the discrepancy between the cluster energy measurement E and the track momentum measurement p comes from an erroneous track momentum measurement. Where erroneous does not necessarily mean straight out wrong, but that the measured track does not carry the full momentum of the initial electron. Firstly, excessive bremsstrahlung losses are always a possibility and secondly remembering the simple model described in 6.1.3, even a correct track momentum measurement in the case of a track from a conversion electron being associated to the calorimeter cluster would result in an unfavorable E/p

value.

Interesting is also the fact that in the case of charge misidentification one sees a relatively high number of E/p values below 1, which would correspond to a track momentum exceeding the cluster energy. This might be caused by additional hits close to the beam axis contributing to the track fit, which are possibly unrelated to the actual electron. Subsections 6.2.2 and 6.2.3 will further discuss this issue.

6.2.2 Association of Reconstructed Tracks to Conversion Electrons

Figure 6.10 displayed the E/p distribution for misidentified electrons and all electrons. The previous section has shown that for charge misidentified electrons the interrelation between the electron cluster energy and the momentum of its track is not given anymore in all generality. This hints towards a previously stated assumption. The particular assumption was, that in the case of the misidentified electrons, a track coming from a conversion electron is associated to the electron cluster. With Monte Carlo data at hand it is possible to try to verify this assumption by attempting to match a Monte Carlo conversion electron to the reconstructed track of a charge misidentified electron.

Also, in figure 6.3 it was shown that in the case of charge misidentified electrons, one often finds a number of reconstructed tracks in the vicinity of the track of the electron that were not associated to a cluster in the electromagnetic calorimeter during reconstruction. It would further support the model of charge misidentification through bremsstrahlung and conversion if it were possible to also match these close tracks to the Monte Carlo electrons from the bremsstrahlung or conversion process.

Conversion Electrons and Reconstructed Track of Charge Misidentified Electrons

The task to be accomplished now is to find the conversion that gives rise to a conversion electron with high enough energy so that its track could be associated to the electron cluster by the reconstruction algorithm. In order for the misidentified electron in such a case to have an E/p value that is in an acceptable range of up to 4, the track momentum of the oppositely charged conversion electron has to be at least one quarter of the cluster energy. The cluster energy is expected to be approximately equal to the energy of the original electron, since bremsstrahlung photons and conversion electrons still contribute to the cluster in the electromagnetic calorimeter because the resolution of the calorimeter is too coarse to resolve these objects. It seems therefore sensible to search for the conversion electron with the highest energy in the bremsstrahlung-conversion cascade, which carries the opposite charge with respect to the original (generator level) electron. For further reference these electrons will be called *LBOC*s (**l**eading electrons from converted **b**remsstrahlung photons with **o**pposite **c**harge). Figure 6.12 shows a schematic depiction of a bremsstrahlung and conversion cascade. For illustration purposes the charge of the generator level electron is arbitrarily chosen to be positive. The bold lines represent the conversion electrons with an opposite charge with respect to the generator level electron. These are the possible candidates for the LBOC. In subsection 4.2.2 it was described that for every Monte Carlo electron information about its ancestor on generator level had been written to the analysis n-tuples. This is indicated by the dashed line in figure 6.12. Therefore a straightforward approach to find the LBOC could be employed:

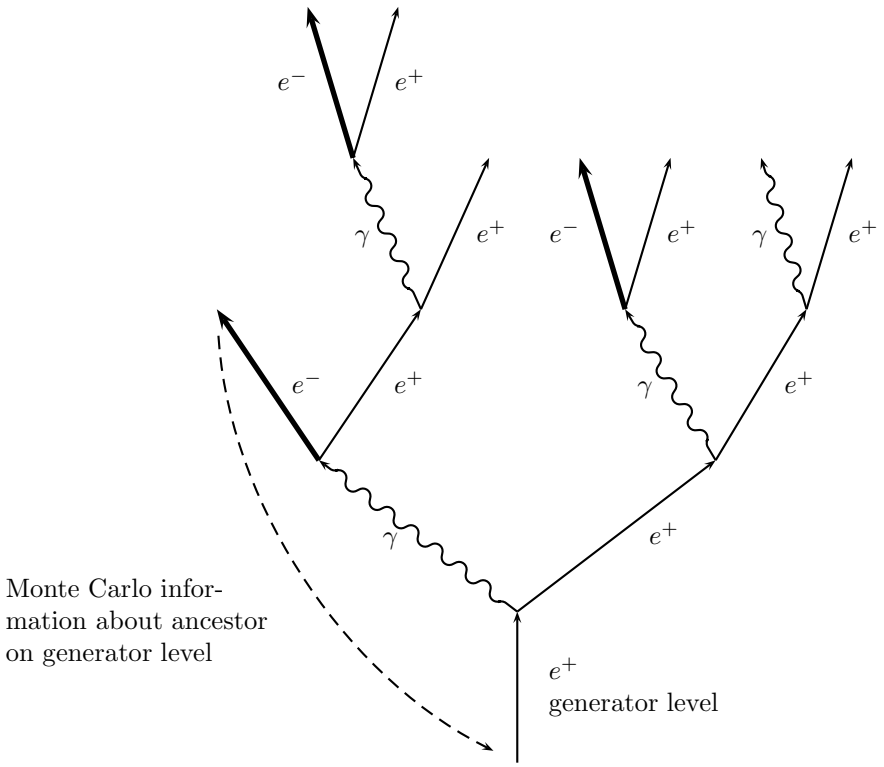

Figure 6.12: Schematic depiction of a bremsstrahlung and conversion cascade. The bold lines represent the conversion electrons with an opposite charge with respect to the generator level parent electron. For every Monte Carlo electron information about its ancestor on the generator level is available, indicated by the dashed line.

1. In an event, select all Monte Carlo electrons having the same common generator level parent.

2. From these select the ones with opposite charge with respect to the generator level parent.

3. Within this selection, find the one with the highest energy.

Figure 6.11 shows the fraction of generator level energy taken by the LBOC. For all electrons one finds that the vast majority (more than 85%) of LBOCs carry energies below 25% of the generator level electron energy. In the case of misidentified electrons however, one sees that the situation is reversed. Most of the LBOCs from misidentified electrons, namely more than 70% carry an energy that is greater than one quarter of the generator level electron energy. As mentioned before this would correspond to an E/p value of 4, given the cluster collects all the energy of the generator electron and the track momentum of the conversion electron is measured correctly.

As indicated it will be tested whether these LBOCs, which correspond to electron '2' in the schematic picture figure 6.4, can be matched to the tracks of the misidentified electrons. A simple ΔR matching in the η-ϕ space is not possible since the tracks and

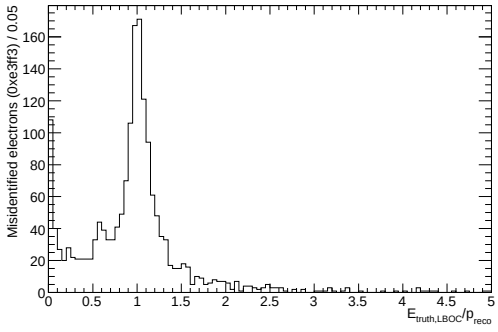

Figure 6.13: Ratio of Monte Carlo truth energy of the LBOC and the reconstructed momentum of the track of the misidentified electron.

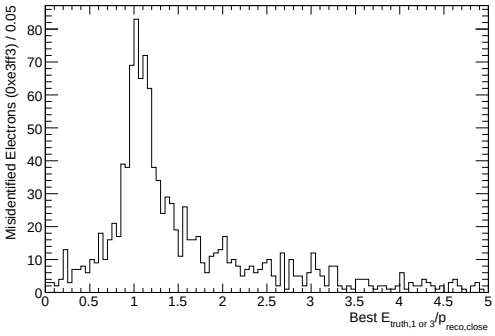

Figure 6.14: Ratio of Monte Carlo truth energy of electrons suspected to be responsible for additional reconstructed tracks and the reconstructed momentum of these tracks for events with one or two nearby tracks.

all the bremsstrahlung products are situated too close to each other and therefore an unambiguous association through spatial variables is not feasible. Therefore the strategy now is to find the LBOC and calculate the ratio

$$\frac{E_{truth}}{p_{track}} \equiv \frac{\text{Monte Carlo truth energy of LBOC}}{\text{Reconstructed momentum of track of misidentified electron}} .$$

Figure 6.13 shows the result for the $Z \to ee$ sample for all charge misidentified electrons. This E_{truth}/p_{track} distribution shows a very high peak at one. This means that there is a large fraction of the misidentified electrons, whose track momentum matches the Monte Carlo energy of the LBOC quite closely. The right tail of the distribution could result from simple bremsstrahlung losses of the conversion electrons. More interesting however is the left hand side of the E_{truth}/p_{track} distribution. Apparently there is also a significant number of LBOCs, whose truth energy is much lower than the track momentum of the misidentified electron. About 28% of the entries in figure 6.13 lie in the range between zero and 0.7. There are two possible explanations:

1. The charge misidentification in these cases has its reasons not in the association of the cluster with a conversion electron track at all, but rather comes from resolution effects and/or kink effects.

2. The track associated to the electron does not entirely consist of the hits from the conversion electron, but also picks up hits from objects before the conversion, as is indicated by the intersection of the track of the original electron and the extrapolated track of the conversion electron in figure 6.4.

In the first case the track momentum of the LBOC has nothing to do with the electron cluster energy at all. The energy of the highest energetic conversion electron does not even need to be anywhere near the energy of the electron. This would explain the high number of entries at very low values in figure 6.13.

In the second case it is mentioned that it is possible for the track of the electron not to consist of only the hits made by one object, but by more than one. Suppose the conversion takes place late in the Pixel detector. While this might still be early enough for an electron associated to this track to be awarded a medium quality, since only a certain number of hits in the Pixel plus SCT trackers are required, it is also possible that the track reconstruction algorithm finds hits earlier in the Pixel detector that are compatible with this track. These hits might be coming from the original generator level electron. In that case the additional hits lead to an increased value of the fitted transverse momentum p_T of the track.

Conversion Electrons and Close Tracks

Figure 6.14 shows the E_{truth}/p_{track} value for the tracks found in the vicinity of the track of the electron, that were not associated to the electron calorimeter cluster during reconstruction. If these tracks come from the same conversion it should be possible to proceed the same way as was done for the electron track. Starting from the bremsstrahlung and conversion found by searching for the LBOC, one can now compare the truth energy of the electrons denoted with '3' and '4' in figure 6.4 to the reconstructed momenta of the nearby tracks. In the cases where only one additional track is found near the track of the electron the momentum of this track is compared to both Monte Carlo electrons and then it is opted for the best E_{truth}/p_{track} value. Analog in the case of two reconstructed nearby tracks the two momenta of the tracks are compared to Monte Carlo electron '3' and '4', and again it is opted for the best E_{truth}/p_{track} value of all combinations.

The result shown in figure 6.14 indicates a good agreement between the reconstructed tracks and the electrons coming from the bremsstrahlung and the conversion, since the distribution peaks sharply at 1.

6.2.3 Transverse Impact Parameter

A parameter that is very sensitive to the track parameters is the transverse impact parameter. It can be used to further test the applicability of the model for charge misidentification through bremsstrahlung and conversion and to check whether the association of an electron from converted bremsstrahlung photon to the reconstructed track of a charge misidentified electron as conducted in the previous subsection is indeed consistent.

The impact parameter in the transverse plane is the point of closest approach of the (extrapolated) track to the beam axis in the transverse (r-ϕ) plane. Figure 6.15 shows the two distributions of d_0 for all electrons and for charge misidentified electrons. The distribution for all electrons peaks at zero and quickly falls off for higher values of d_0. The range shown for d_0 in the figure is from 0 to 1 mm, since 1 mm is the cut value applied for medium and tight electrons. (See Bit 19, TrackA0 in the `El_IsEM` flag.) This means that for medium and tight electrons the value of d_0 is required to be less than 1 mm. Greater values indicate that the object might not originate from the interaction point, or at least something went wrong during reconstruction. The distributions in figure 6.15 indicate however, that electrons are usually well within this value and even a cutoff parameter as low as 0.2 mm would decrease the reconstruction efficiency only by about 3%.

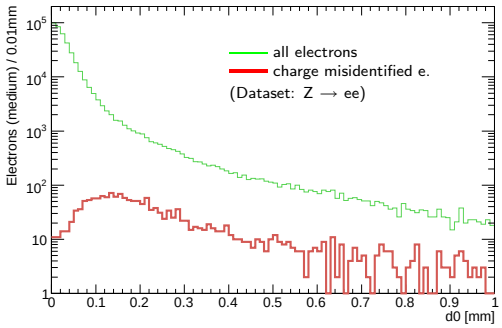

Figure 6.15: Impact parameter in the transverse plane d_0.

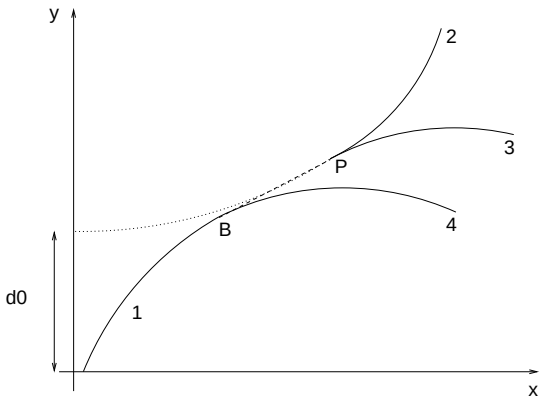

Figure 6.16: Schematic picture of transverse impact parameter.

The picture looks different for charge misidentified electrons. Their d_0 distribution has a shallow peak at around 0.15 mm that falls off to the left more quickly than to the right. Only 53% of misidentified electrons are within $d_0 \leq 0.2\,\text{mm}$.

A possible explanation is schematically shown in figure 6.16. This depiction is exaggerated for illustration purposes and is not drawn to scale. It basically repeats the scenario for electron charge misidentification through bremsstrahlung and conversion from figure 6.4 in the transverse plane. Starting with the generator level electron denoted with '1' and a small impact parameter, eventually bremsstrahlung (at point B) and conversion (at point P) take place, resulting in the oppositely charged conversion electron '2', whose track is associated to the calorimeter cluster, leading to charge misidentification. Extrapolating the oppositely curved track of electron '2' backwards, yields its point of closest approach to the beam axis. This would correspond to the reconstructed value of d_0 if in this case charge misidentification actually works the suggested way.

In order to verify the scenario, the track of the Monte Carlo electron '2', which corresponds to the LBOC was extrapolated by hand and the results were compared to the value for d_0 from the reconstruction. To this end, the Monte Carlo energy of electron '2' and its η value will be used to calculate the radius of its track in the magnetic field B of the Inner Detector.

$$R = \frac{1}{c} \cdot \frac{p_T}{B} = \frac{1}{c} \cdot \frac{E}{B\cosh(\eta)} \tag{6.1}$$

This yields the radius of the track in mm. Then with the vertex information (x_0, y_0) of Monte Carlo electron '2' and its ϕ coordinate at the point of its production P, one gets the center point (c_1, c_2) of the circle, of which the track is a segment:

$$\begin{pmatrix} c_1 \\ c_2 \end{pmatrix} = \begin{pmatrix} x_0 \\ y_0 \end{pmatrix} + R\,q \cdot \begin{pmatrix} \sin(\phi) \\ \cos(\phi) \end{pmatrix} \tag{6.2}$$

The expected value for the transverse impact parameter is then calculated as the distance of the center point of the circle minus its radius:

$$d_{0,exp} = \left| \begin{pmatrix} c_1 \\ c_2 \end{pmatrix} \right| - R = \sqrt{c_1^2 + c_2^2} - R \tag{6.3}$$

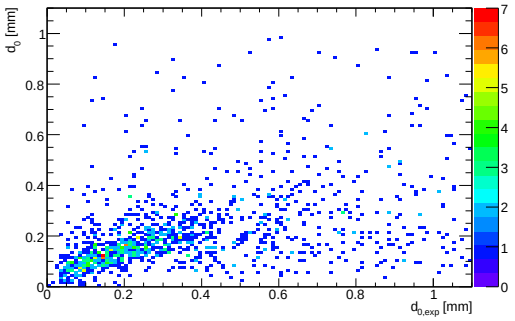

Figure 6.17: Reconstructed d_0 versus calculated $d_{0,exp}$ based on Monte Carlo data. Correlation factor $\rho = 0.451$.

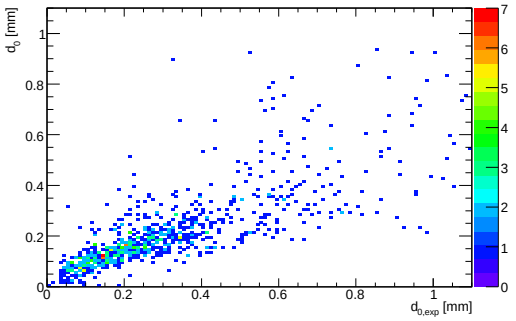

Figure 6.18: Reconstructed d_0 versus calculated $d_{0,exp}$ based on Monte Carlo data for $0.9 \leq E_{truth}/p_{track} \leq 1.4$. Correlation factor $\rho = 0.779$.

If the charge misidentification actually comes from associating the track of conversion electron '2' with the electron cluster and the track of the conversion electron is cleanly reconstructed, i.e. it does not contain hits from other objects, the reconstructed d_0 should correspond to the value of $d_{0,exp}$ expected from the Monte Carlo information. A plot of the actual reconstructed value of d_0 versus the calculated $d_{0,exp}$ is shown in figure 6.17. While the actual value of d_0 is somewhat overestimated by $d_{0,exp}$, there is a clear correlation between the reconstructed and calculated value. The correlation factor calculated to $\rho = 0.451$. The bulk of events is found near the diagonal, but there is also a number of events with $d_0 \gg d_{0,exp}$ and $d_0 \ll d_{0,exp}$. The events expected to fit the simple model well, would be the misidentification events with a cleanly reconstructed track of the oppositely charged conversion electron, whose momentum matches the truth energy of the Monte Carlo electron. These correspond to the events from figure 6.13 with an acceptable E_{truth}/p_{track} value of within 0.9 and 1.4. Figure 6.18 shows the relation between reconstructed d_0 and calculated $d_{0,exp}$ for these events. As expected, d_0-$d_{0,exp}$ pairs far off the diagonal disappear and the correlation factor ρ increases to 0.779.

About 37% of electron tracks start in the Pixel layers while Monte Carlo data suggests that the conversion takes place later in the SCT tracker. Therefore these tracks must pick up hits that lie closer to the beam axis from other objects, that are also considered during the fit and thus leading to a wrong track momentum measurement. These cases correspond roughly to the entries below the diagonal in the $d_{0,exp} - d_0$ plot, where $d_{0,exp}$ overestimates the actual reconstructed d_0. Through the additional hits considered for the track fit the reconstructed d_0 becomes smaller since the electrons responsible for the additional hits come from the actual interaction point. Figure 6.19 shows the two-dimensional histogram of reconstructed d_0 versus $d_{0,exp}$ for all misidentified electrons with a E_{truth}/p_{track} value of less than 0.9. Almost all entries lie below the diagonal, backing the assumption that additional hits close to the beam axis considered for the fit lead to a higher track momentum. This is further supported by figure 6.20, where the radial distance from the beam axis of the production versus decay vertices of the bremsstrahlung photons responsible for the corresponding LBOCs is shown. The bulk of bremsstrahlung

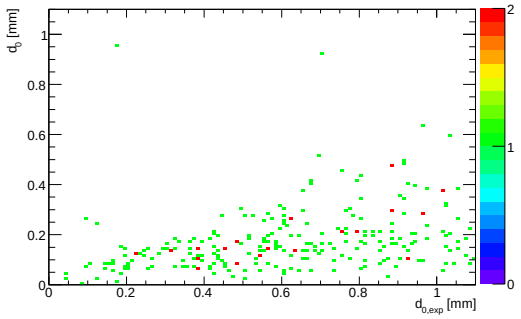

Figure 6.19: Reconstructed d_0 versus transverse impact parameter from Monte Carlo information $d_{0,exp}$ for $E_{truth}/p_{track} \leq 0.9$.

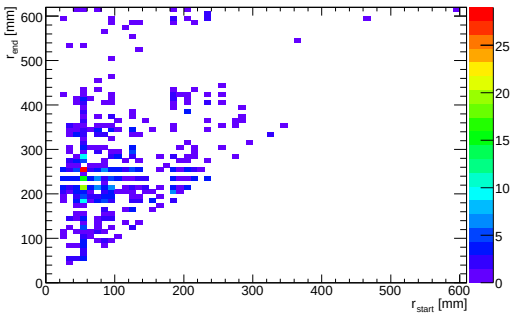

Figure 6.20: Bremsstrahlung photon end vertex radius (conversion) versus start vertex radius (bremsstrahlung) for $E_{truth}/p_{track} \leq 0.9$.

photons is not converted until the SCT tracker at radii greater than 200 mm and only very few bremsstrahlung photons originate from the first layer of the Pixel tracker at all, most come from the second layer at around 55 mm. Since however medium electron candidates are required to have a minimum number of hits in the Pixels, these hits cannot come from the LBOC. In the case of isolated electrons it seems likely that these hits are generated by the original electron before emitting the hard bremsstrahlung photon. Figure 6.7 displayed earlier, shows the bremsstrahlung photon production and conversion radii with no restriction on the E_{truth}/p_{track} of the LBOC. There, in contrast to figure 6.20 most bremsstrahlung photons are generated and converted within the Pixel tracker.

Points that lie well above the diagonal in the d_0-$d_{0,exp}$ plot, correspond mostly to bremsstrahlung photons generated and converted in the first two layers of the Pixel detector. They can be identified with the LBOCs that have a E_{truth}/p_{track} value of greater than 1.4. Possibly they are subject to bremsstrahlung losses along the way through the detector leading to their increased E_{truth}/p_{track}. Bremsstrahlung losses could also explain an increased d_0 value, since in the presence of bremsstrahlung the track becomes more curved, which in an extrapolation in the transverse would lead to a higher estimate for the transverse impact parameter.

6.2.4 Charge Misidentification at Very High Transverse Momentum

Up until now primarily the electron charge identification in a low p_T region of electrons compared to the energies present at ATLAS was of concern. In the $Z \rightarrow ee$ sample electrons are kinematically confined mostly to the p_T region below half the Z^0 mass, around 45 GeV, since the Z^0 are mainly produced with low p_T. The main publication on the ATLAS detector [4] states numbers for the electron charge misidentification probability shown in the plot in figure 6.21. Figure 6.22 shows the charge misidentification rate in several single electron samples at approximately the same p_T values as used in the plot from the detector paper, using the definition 5.1. While for the very high p_T range the numbers seem to be in agreement there is a discrepancy of up to about one

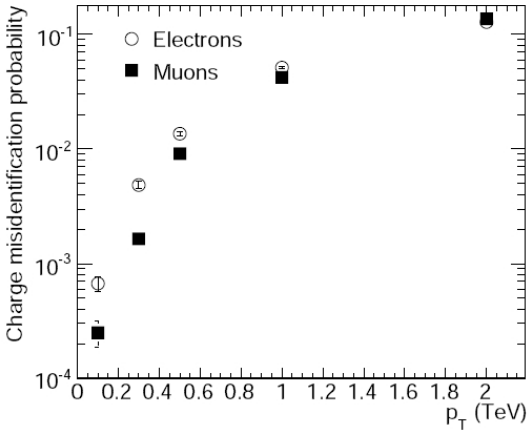

Figure 6.21: Charge misidentification probability for muon and electron tracks from [4].

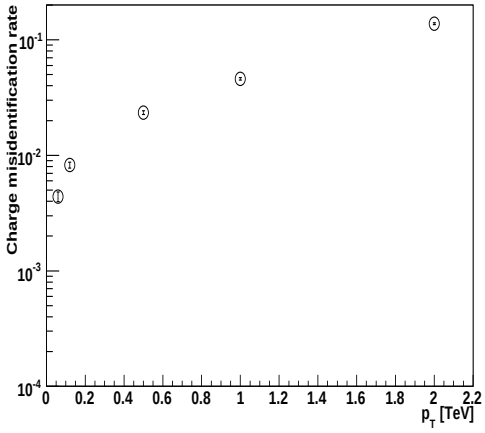

Figure 6.22: Charge misidentification rate for several single electron samples at different transverse momenta, calculated with definition 5.1.

order of magnitude for the lower p_T end of the plots. The numbers from the detector paper are considerably lower.

The way the numbers for charge misidentification probability are calculated in the detector paper are incompatible with the definition of charge misidentification given in this thesis. The procedure in the detector paper was as follows:

1. A single electron sample was used and events with exactly one reconstructed track were chosen.

2. Only tracks with more than 80% of its hits coming from the same Monte Carlo truth particle were considered.

3. A cut on the barcode of the truth particle was applied, such that electrons from conversions of bremsstrahlung photons were not considered.

There is no electron identification involved at all, since these definitions were initially aimed at studying and optimizing the reconstruction of tracks. With the above selection criteria only charge misidentification events due to too low resolution of the detector and from kinks in the electron track as a result of an occurrence of bremsstrahlung are considered. It was however postulated in the sections above that these are not the main reasons for charge misidentification according to definition 5.1, which seems sensible at least from a physics analysis point of view. Charge misidentification from associating a track of a conversion electron to a calorimeter cluster cannot be measured when the above criteria are applied.

Interestingly with increasing transverse momentum, numbers from both methods converge. This must mean that charge misidentification from conversion effects contributes less to the total number of charge misidentification at high transverse momentum than

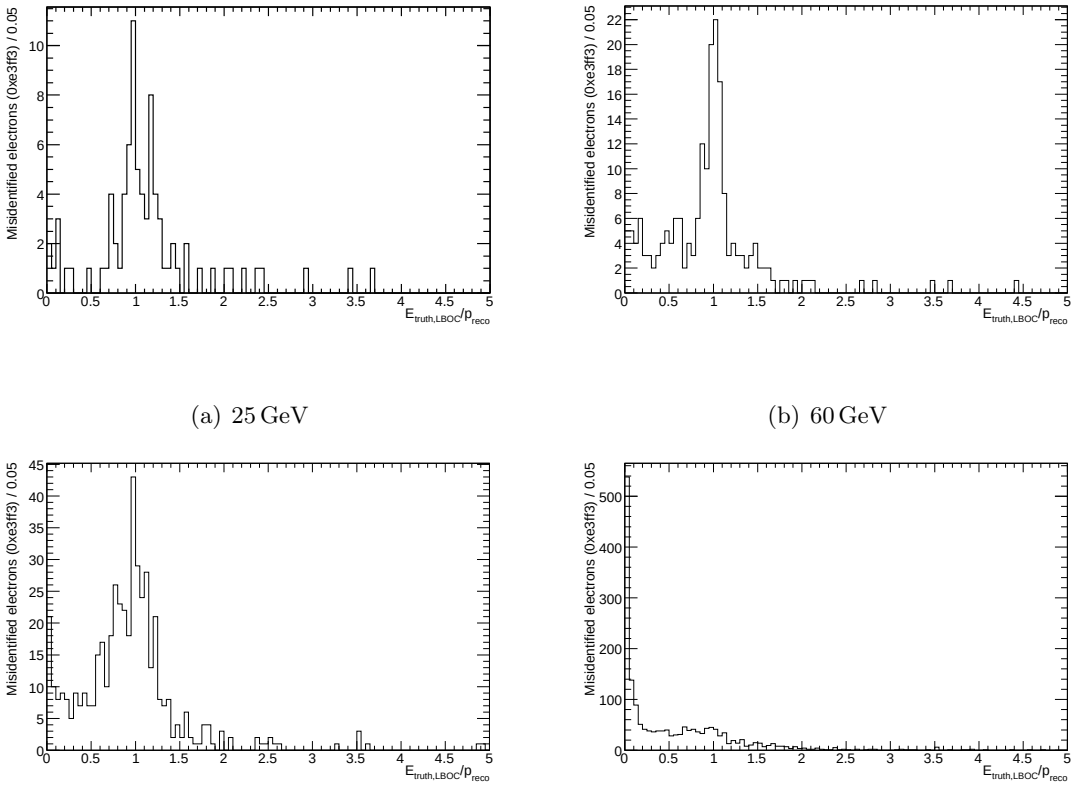

(a) 25 GeV

(b) 60 GeV

(c) 120 GeV

(d) 500 GeV

Figure 6.23: Ratio of the Monte Carlo truth energy of the LBOC and the reconstructed momentum of the track of the misidentified electron for several values of electron transverse momentum. Single electron samples were used.

it does in the low p_T region. Figures 6.23 (a) through (d) show the ratio of the Monte Carlo truth energy of the LBOC and the momentum of the track that is associated to the electron candidate for several single electron samples at different transverse momenta for charge misidentified electrons. This ratio was shown for the $Z \rightarrow ee$ sample in 6.13. Figures 6.23 (a) and 6.13 look very similar. That is expected because the transverse momenta are in the same range in both cases and the $Z \rightarrow ee$ physics sample is probably as close as one can get with a physics sample to a single electron sample. Here again one finds the sharp peak around 1, which means that indeed in a high number of cases of charge misidentification the track associated to the misidentified electron corresponds to the Monte Carlo energy of a conversion electron. The relative height of this peak can be seen as a measure of how big the contribution from misidentification through conversion actually is, compared to the other possible sources for charge misidentification. As the transverse momentum increases, one can clearly see this peak around 1 broadening (c) and disappearing at very high p_T (d).

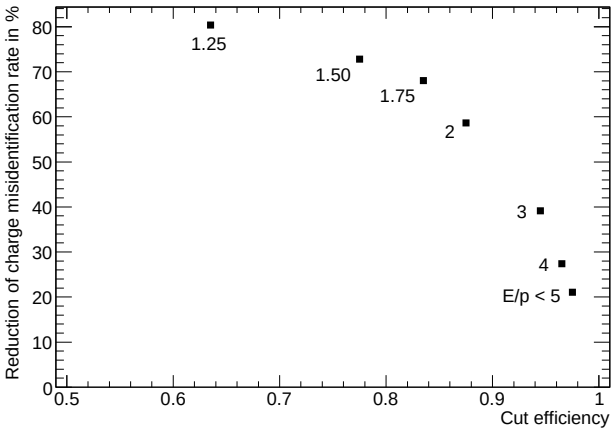

Figure 6.24: Reduction of charge misidentification rate versus cut efficiency for several cut values for the E/p variable. Electrons with $E/p < 0.7$ and a E/p value greater than the cut value are rejected.

6.3 Consequences and Possible Countermeasures

In the previous sections it was shown that a large source for electron charge misidentification are bremsstrahlung and conversion processes. In the case of charge misidentification one tends to see higher track multiplicities in reconstructed events and can associate those tracks to the Monte Carlo constituents of the bremsstrahlung and conversion process. The high contribution of bremsstrahlung to charge misidentification processes has some consequences seen in a number of reconstruction variables. These supply some handles to reduce the charge misidentification rate.

6.3.1 Cluster Energy over Track Momentum – E over p

As already stated in subsection 6.2.1, E/p is a standard reconstruction variable used to determine the quality of the reconstructed electron. Ideally the energy deposited in the calorimeter, E, and the momentum of the reconstructed track, p, should be equal. With the presence of bremsstrahlung losses on the way through the detector material, the track momentum is lower than the energy collected in the calorimeter cluster most of the times. Since it was shown that the greatest part of charge misidentified electrons suffers from catastrophic bremsstrahlung and conversion effects, E/p provides some handle to cut down on the charge misidentification rate. Figure 6.10 shows the distribution of E/p for all electrons and for charge misidentified electrons. For the price of losing some electron reconstruction efficiency the misidentification rate can be reduced by rejecting electrons with high E/p values, since the bulk of reconstructed electrons can be found at E/p values near 1. The plot in figure 6.24 shows the reduction of the charge misidentification rate versus the cut efficiency. The cut efficiency is defined as the ratio of electrons passing the cut and the number of electron reconstructed without the cut being applied. The

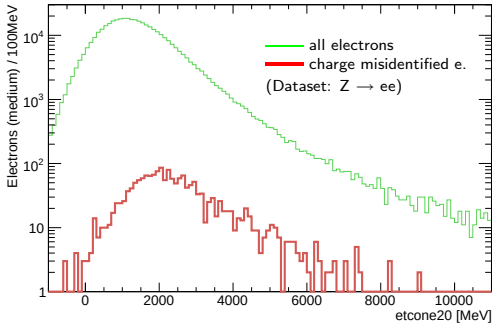

Figure 6.25: The value of the etcone20 variable for all medium electrons in the $Z \rightarrow ee$ sample and for charge misidentified electrons only.

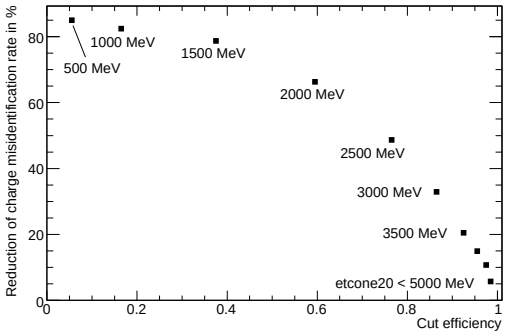

Figure 6.26: Cut efficiency versus reduction of charge misidentification rates for several cut values. Electron candidates with etcone20 values greater than the cut value are rejected.

reduction of the charge misidentification rate is given by the expression $1 - \lambda_{\text{cut}}/\lambda_{\text{nocut}}$, where λ_{cut} and λ_{nocut} are the charge misidentification rates with the cut applied and with no cut applied, respectively.

For example, requiring the E/p value to be less than 2 (and greater than 0.7) the charge misidentification rate is reduced by about 60%, while still more than 85% of electrons pass the cut.

6.3.2 Transverse Energy around the Electron Cluster – etcone20

The etcone20 variable is a standard reconstruction variable, that holds the transverse energy within a cone of radius $\Delta R = 0.20$ around the direction of the reconstructed particle minus the transverse energy of the particle itself. The transverse energy, E_T, is defined as $E_T = E \cdot \sin(\theta)$, where θ is the angle of the particle track with the beam axis. This way the etcone20 variable can be used to determine how spatially isolated a reconstructed object is. This helps especially rejecting jets from being reconstructed as electrons.

Since it was shown that charge misidentified electrons suffer more severely from bremsstrahlung, one could expect that the energy deposits in the electromagnetic calorimeter are less concentrated than in the general case, where on average there are less bremsstrahlung photons and conversion electrons. This 'spraying' of energy for misidentified electrons should be represented by an increased value of etcone20. Figure 6.25 shows the distribution of the etcone20 reconstruction variable for all medium electrons in the $Z \rightarrow ee$ sample and for the charge misidentified medium electrons. As expected the distribution for the charge misidentified electrons is somewhat shifted to higher values of etcone20. Accepting etcone20 values of up to 2500 MeV, about 50% of the misidentified electrons would be cut away while about 25% of all reconstructed electrons would be lost. A plot of the cut efficiency, i.e. the fraction of reconstructed electrons that pass the cut, versus the reduction of the electron charge misidentification at several cut values

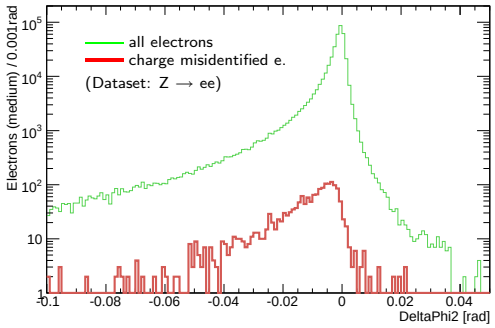

Figure 6.27: The value of the deltaPhi2 variable for all medium electrons in the $Z \rightarrow ee$ sample and for charge misidentified electrons only.

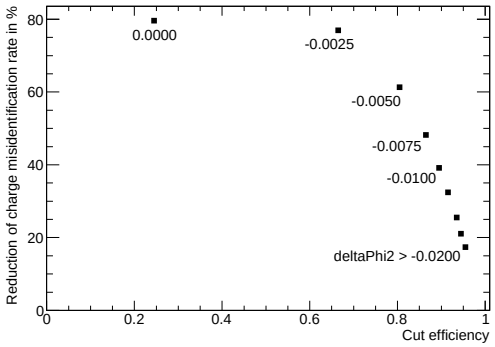

Figure 6.28: Cut efficiency versus reduction of charge misidentification rates for several cut values. Electron candidates with deltaPhi2 values less than the cut value are rejected.

for etcone20 is shown in figure 6.26. Electron candidates with an etcone20 value greater than the cut value are rejected. The overall performance of this distinction method is not overwhelming. Cutting on etcone20 can help to reduce the charge misidentification rate, however for values below 2500 MeV the cut efficiency is diminished at a much greater rate than the charge misidentification probability.

6.3.3 Difference between Cluster Phi and Track Phi – deltaPhi2

The reconstruction variable deltaPhi2 describes the difference between the cluster ϕ position and the ϕ coordinate of the track extrapolated to the second layer of the calorimeter. The sign of this variable depends on the charge, i.e. the curvature, of the track candidate. If the track is curved towards the cluster position the sign of deltaPhi2 is positive and oppositely if the track is curved away from the cluster position the sign of deltaPhi2 is negative. An electron that passes through the detector and does not suffer from bremsstrahlung will have a deltaPhi2 value of 0 if the track of this electron is perfectly measured, i.e. the position of the cluster in the electromagnetic calorimeter and the extrapolation of the electron track match exactly (in the r-ϕ plane). With bremsstrahlung photons and conversion electrons produced along the way of the electron through the detector, contributing to the total cluster energy, the center of the cluster might be shifted along ϕ, as well as the associated track will have a lower transverse momentum due to those bremsstrahlung losses and such is also shifted along ϕ, but in the opposite direction. This is especially true in the case of charge misidentification through bremsstrahlung and conversion as it was described in the earlier sections. The distribution of deltaPhi2 is shown in figure 6.27 for all electrons and for the charge misidentified electrons in the $Z \rightarrow ee$ sample, which satisfy the medium IsEM quality criteria. The distribution for all electrons shows a sharp peak around 0 which sharply falls to the right and has a somewhat longer tail to the left. This tail is caused by bremsstrahlung. The disagreement of cluster position and track extrapolation is more prevalent among charge

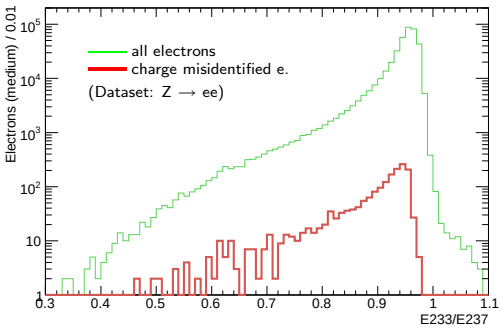

Figure 6.29: The value of E233/E237 for all medium electrons in the $Z \rightarrow ee$ sample and for charge misidentified electrons only.

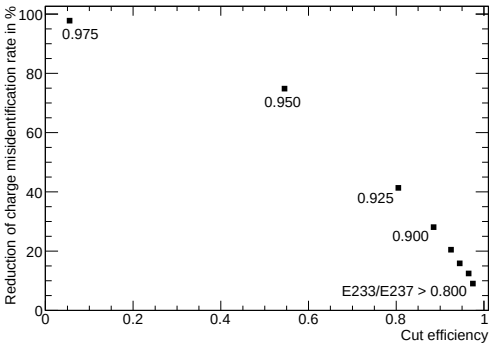

Figure 6.30: Cut efficiency versus reduction of charge misidentification rates for several cut values. Electron candidates with E232/E237 values less than the cut value are rejected.

misidentified electrons. So for example rejecting values for deltaPhi2 of less than -0.005 will result in 80% percent cut efficiency while the number of misidentified electrons is cut by 60%. Figure 6.28 displays the overall cut efficiencies versus the reductions in charge misidentification rate for several cut values of deltaPhi2.

6.3.4 Energies in Differently Sized Calorimeter Cells – E233/E237

The same reasoning as in the previous two subsections is applied here. Electrons that are charge misidentified are subject to higher bremsstrahlung and conversion activity. Bremsstrahlung photons and conversion electrons will lead to dispersion of the energy of the generator level electron along the direction of ϕ. Among the standard reconstruction variables there are several variables describing the energies collected in the second layer of the electromagnetic calorimeter for different arrangements of calorimeter cells. They are called E2$n_\eta n_\phi$, where n_η and n_ϕ stand for the number of cells in the η and ϕ direction respectively. The value is calculated around the center of the calorimeter cluster. Here it will be looked at the ratio of two variables, namely E233 and E237. These are the energies in the second layer of the electromagnetic calorimeter in a 3×3 and a 3×7 cell arrangement respectively. In the case of the energy being dispersed along the ϕ direction E237 is expected to collect considerably more energy than E233. For charge misidentified electrons which are supposed to be suffering from severe bremsstrahlung losses the ratio of E233 and E237 should then be lower than the same ratio for electrons not being subject to hard bremsstrahlung. The distribution of the E233 over E237 ratio for both cases is depicted in figure 6.29. The distribution for all electrons is sharply peaked below 1 with a steep fall and somewhat more shallow rise. Comparing this distribution to the one for charge misidentified electrons one sees that its peak is found at a somewhat lower value and that the rise is even more shallow. Requiring the ratio of E233 and E237 to stay above 0.925 the cut efficiency is reduced by 20% while the charge misidentification rate is reduced by about 40%. Figure 6.30 shows the cut efficiency versus the reduction in

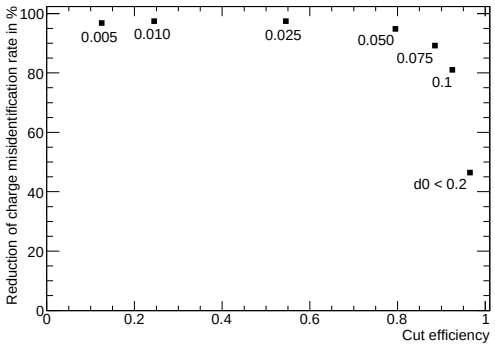

Figure 6.31: Cut efficiency versus reduction of charge misidentification rate for several cut values for the transverse impact parameter d_0. Electron candidates with d_0 values above the cut value are rejected.

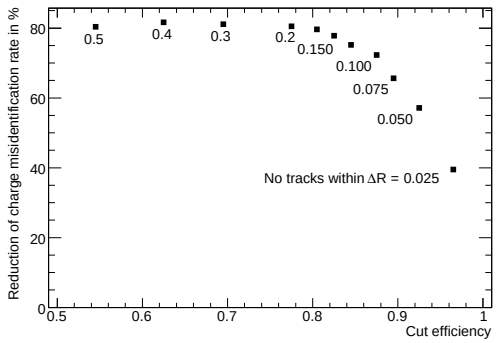

Figure 6.32: Cut efficiency versus reduction of charge misidentification rate for several cut values for the distance within which track isolation is required, i.e. no additional tracks with a p_T greater than 500 MeV are allowed.

charge misidentification rate for a number of different cut values for E233/E237.

6.3.5 Transverse Impact Parameter – d0

The transverse impact parameter d_0 was described in detail in subsection 6.2.3. It shows distinct distribution shapes for the cases of all electrons and charge misidentified electrons (see figure 6.15). Of course this property can be used to discriminate between correctly identified electrons and charge misidentified electrons. For example requiring d_0 to be below a value of 0.1 mm yields an overall cut efficiency of 90% while reducing charge misidentified electrons by about 80%. Compared to the other methods described above this is the most effective way to reduce the charge misidentification rate.

6.3.6 Track Isolation

Another property of charge misidentified electrons that was discussed in subsection 6.1.2 is the fact that one sees a higher track multiplicity than one sees on average for all reconstructed electrons. Requiring that there are no additional tracks with a transverse momentum greater than 500 MeV within a certain distance ΔR around the track of the electron proves to be a very effective measure to reduce the charge misidentification rate. Figure 6.32 shows the overall cut efficiency versus the cut value for ΔR. With a value of $\Delta R = 0.1$ a reduction of the charge misidentification rate of more than 70% can be achieved at a cut efficiency of better than 85%. This is also a very effective way of reducing the charge misidentification probability.

7 Measuring Electron Charge Misidentification

7.1 A Simple Tag-and-Probe Method

While the previous chapters were concerned with understanding the properties of electron charge misidentification looking at Monte Carlo data, it will now be looked at a possibility of how to determine the charge misidentification rate from actual data. A standard approach to this problem is the so-called tag-and-probe method on a $Z \to ee$ dataset. The Z^0 boson decays into two electrons, e^+ and e^- with a charge sum of zero, due to electric charge conservation. If it is possible to acquire a clean $Z \to ee$ sample and if it is further possible to tag one of the two electrons from the decay as certainly correctly identified, then one knows the charge of the other electron prior to and independently from its reconstruction. Comparing this knowledge to the reconstruction result then yields if the charge of the electron in question was correctly or incorrectly identified.

Having selected a clean sample of $Z \to ee$ events and a suitable class of tag electrons whose, misidentification rate is sufficiently low, i.e. considerably lower than the misidentification rate of the probe electrons, the charge misidentification rate can be measured by simply counting the number of same sign and opposite sign tag-and-probe events. The charge misidentification rate of the probe electrons λ_p is calculated by

$$\lambda_p = \frac{N_{ss}}{N_{os} + N_{ss}}\,, \tag{7.1}$$

where N_{ss} is the number of same sign events and N_{os} is the number of opposite sign tag-and-probe events. Assuming for the moment the tag misidentification rate is zero, equation 7.1 is exact, since then the number of same-sign events is equal to the number of misidentified probes and the sum of N_{os} and N_{ss} is just the total number of tag-and-probe events. Equation 7.1 then becomes the naïve equation for the charge misidentification rate λ:

$$\lambda = \frac{N_{misid}}{N_{all}} \tag{7.2}$$

Care must be taken during counting. Events where both electrons satisfy the tag and the probe conditions both electrons have to be counted as a valid probe.

The selection of tag-and-probe pairs from the $Z \to ee$ sample is done in two steps. First events were chosen which had two electrons passing the minimum quality criteria of a loose electron (`El_IsEM` & 0xf3 = 0) and that were additionally required to have a dielectron mass that matched the Z^0 mass, m_Z, within at least 10 GeV. If in one event more than one pair of reconstructed electrons could be found that were within the 10 GeV range around m_Z, then the one with the closest matching dielectron mass was chosen. The dielectron mass was calculated from the energies of the two electrons and the angle between them:

$$m_{ee} = \sqrt{2E_1E_2\,(1 - \cos\alpha)}\,, \qquad \cos\alpha = \frac{\mathbf{p}_1 \cdot \mathbf{p}_2}{|\mathbf{p}_1|\;|\mathbf{p}_2|}\,, \tag{7.3}$$

with $\mathbf{p}_{1,2}$ being the three-momenta of the electrons. In a second step the tag and the probe cuts where applied to the such selected two electrons.

So far it has only been looked at the overall charge misidentification rate with no binning, for example in η. Often one would like to be able to measure the misidentification rate within a number of kinematic bins, like transverse momentum, p_T, or pseudorapidity, η. Generally the above procedure remains the same, equation 7.1 must be evaluated in each bin, with N_{ss} and N_{os} being accounted for separately for each probe bin.

Table 7.1 gives an overview of the results of the simple tag-and-probe method. For the tag electrons a tight IsEM was required in addition to the requirement of no additional track within a distance of $\Delta R = 0.1$ around the track belonging to the electron (see section 6.3.6). The probe electrons satisfy a medium IsEM cut. In addition all electrons are subject to a cut on the transverse momentum of $p_T > 10\,\mathrm{GeV}$. The error given for the charge misidentification rates are the statistical errors according to the 1σ binomial proportion confidence interval given by

$$\sigma = \sqrt{\frac{\lambda\ (1-\lambda)}{N_{ss}}}\,. \tag{7.4}$$

The Monte Carlo rates where determined by simply looking at all electrons within a given bin that satisfy the probe conditions and looking at the Monte Carlo charge information of the matched truth electron. Therefore the sets of electrons used to determine the Monte Carlo rates and the tag-and-probe rates are not identical. It is assumed that the class of probe electrons is a good representation of all electrons that do fulfill the probe cuts, whether they have a tag partner or not. Therefore selection effects might lead to discrepancies between the numbers returned by the tag-and-probe and Monte Carlo measurements. Comparing the values of the Monte Carlo misidentification rate and the rates from the tag-and-probe method, one sees that except for the last bin the tag-and-probe charge misidentification probability, λ_p, overestimates the actual Monte Carlo misidentification rate $\lambda_{p,MC}$ in the sample.

One possible explanation for this behavior is, that the tag misidentification rates were

Table 7.1: Results of the simple tag-and-probe method from $Z \to ee$ with tag charge misidentification rates assumed to be zero. A transverse momentum cut $p_T > 10\,\mathrm{GeV}$ is applied for all electrons. Tag electrons are tight electrons with a required track isolation within $\Delta R \leq 0.1$. Probe electrons are medium electrons. The Z^0 is reconstructed from events with two electrons having a dielectron mass m_{ee} with $|m_{Z^0} - m_{ee}| \leq 10\,\mathrm{GeV}$.

η bin	N_{os}	N_{ss}	$\lambda_p\,/\,10^{-3}$	$\lambda_{p,MC}\,/\,10^{-3}$
$0 \leq \eta < 2.5$	136857	522	3.80 ± 0.17	3.37
$0 \leq \eta < 0.5$	38485	36	0.93 ± 0.16	0.65
$0.5 \leq \eta < 1.0$	35661	42	1.18 ± 0.18	0.90
$1.0 \leq \eta < 1.5$	27891	91	3.25 ± 0.34	1.98
$1.5 \leq \eta < 2.0$	18829	122	6.44 ± 0.58	5.87
$2.0 \leq \eta < 2.5$	15991	231	14.24 ± 0.93	14.43

not considered. In the tag-and-probe ansatz above a charge misidentified tag electron leads to a same sign event and is thus counted as a misidentified probe and contributes to the probe misidentification rate. The reason for this effect not being prevalent in the last bin is twofold. Firstly the probe misidentification rate in this bin is the highest of all bins, due to the η dependence of the charge misidentification rate. Therefore nonzero tag misidentification rates should have the least impact in this bin. Secondly in this highest η bin a lot of the electrons come from a Z^0 that is highly boosted along the z-axis. It is not unlikely that only one electron from the Z^0 decay is reconstructed while the other has a η value greater than 2.5 and therefore cannot be reconstructed by the ATLAS detector. Thus they cannot be included in the tag-and-probe analysis. These electrons are however counted for the calculation of the Monte Carlo charge misidentification rate and due to the fact that they have a high η, they are relatively likely to be charge misidentified.

In the η region between 1.37 and 1.52 the electron identification and energy measurement are degraded because of the large amount of material in front of the calorimeter [21]. In this region, i.e. in the third η bin ($1.0 \leq \eta < 1.5$), clearly a higher discrepancy between the charge misidentification rate determined by the tag-and-probe method and the rate calculated from Monte Carlo data is seen.

7.2 Tag-and-Probe with Tag Misidentification Rates

Up to this point the effect of nonzero tag charge misidentification rates was neglected. They might however play an important role, especially in the cases where the probe electron is in one of the lower η bins, where the charge misidentification rate is relatively low. If in such a case the tag electron is found at higher η values then it might have a charge misidentification probability that is not negligible anymore. In the following a basic assumption about the tag-and-probe misidentification rates is made, which was implicitly already made in the previous section. It is assumed that the charge misidentification probabilities for an electron in one bin do not depend on the bin, the corresponding tag electron is in. Then in order to incorporate the tag misidentification rates, λ_t, one has to keep record of the number of tag electrons that fall into a certain bin, for each bin of probe electrons. So for each probe bin b, the number of tag electrons, $N_t(d;b)$, that fall into a certain tag bin d, as well as the tag misidentification rates, $\lambda_t(d)$, in tag bins d are known. The expected number of same sign events in a bin b is then given by

$$N_{ss}(b) = \lambda_p(b)\, N_p(b) + \sum_d \lambda_t(d)\, N_t(d;b) \ . \tag{7.5}$$

The sum over the tag misidentification rates divided by the total number of tag electrons can be viewed as an average tag misidentification rate

$$\bar{\lambda}_t(b) = \frac{1}{N_t} \sum_d \lambda_t(d)\, N_t(d;b) \ , \tag{7.6}$$

for each probe bin b. Thus equation 7.5 can be written as

$$N_{ss}(b) = \lambda_p(b)\, N_p(b) + \bar{\lambda}_t(b)\, N_p(b) \ , \tag{7.7}$$

since the total number of tags, N_t, is equal to the total number of probes, N_p. The probe misidentification rates are then calculated by:

$$\lambda_p(b) = \frac{N_{ss}(b)}{N_p(b)} - \bar{\lambda}_t(b) \tag{7.8}$$

This is essentially equation 7.1 except for a correction term $-\bar{\lambda}_t$ that takes the tag misidentification rates into account. A method for determining sensible values for the tag misidentification rates will be discussed in the next section. Table 7.2 shows the result of the tag-and-probe analysis carried out with considering tag charge misidentification rates from section 7.3. The numbers are in better agreement now with the Monte Carlo data than the values in table 7.1.

7.3 Determining the Tag Charge Misidentification Rate

In the simple tag-and-probe ansatz we assumed the charge misidentification rate for the tag electron to be zero. In order to get to a more accurate measurement of the charge misidentification rate of the probe electrons the tag misidentification probability has to be evaluated. Since it is not possible to introduce a class of electrons that is even less subject to charge misidentification than the tag electrons for practical and statistical reasons it has to be thought of another method.

Information on the charge misidentification rate of the tag electrons can also be gained from looking at tag-tag events and in the most general case information from all possible pairings, tag-tag, tag-probe and probe-probe can be taken into account. However in this approach we are not as flexible in choosing cuts for the probe electron as in a simple tag-and-probe approach. All electrons are therefore divided in two disjoint sets of tag electrons and non-tag electrons. This way it is possible to independently determine the charge misidentification rates for tag electrons. The stringent separation avoids double counting issues and thus especially allows a sensible error estimation by the fit algorithm employed below.

Table 7.2: Results of the simple tag-and-probe method from $Z \to ee$ with tag charge misidentification rates assumed to be nonzero. A transverse momentum cut $p_T > 10\,\mathrm{GeV}$ is applied for all electrons. Tag electrons are tight electrons with a required track isolation within $\Delta R \leq 0.1$. Probe electrons are medium electrons. The Z^0 is reconstructed from events with two electrons having a dielectron mass m_{ee} with $|m_{Z^0} - m_{ee}| \leq 10\,\mathrm{GeV}$. For the tag charge misidentification rates λ_t used see table 7.3.

η bin	$\bar{\lambda}_t \,/\, 10^{-3}$		$\lambda_p \,/\, 10^{-3}$		$\lambda_{p,MC} \,/\, 10^{-3}$
$0 \leq \eta < 0.5$	0.29	$^{+0.14}/_{-0.10}$	0.64	$^{+0.30}/_{-0.26}$	0.65
$0.5 \leq \eta < 1.0$	0.30	$^{+0.14}/_{-0.10}$	0.87	$^{+0.32}/_{-0.29}$	0.90
$1.0 \leq \eta < 1.5$	0.32	$^{+0.15}/_{-0.11}$	2.94	$^{+0.49}/_{-0.45}$	1.98
$1.5 \leq \eta < 2.0$	0.36	$^{+0.16}/_{-0.12}$	6.08	$^{+0.74}/_{-0.70}$	5.87
$2.0 \leq \eta < 2.5$	0.39	$^{+0.17}/_{-0.13}$	13.86	$^{+1.10}/_{-1.06}$	14.43

Electron pairs from the Z^0 decay are binned in a 10 by 10 histogram in 5 η bins each for tag and non-tag electrons. Same sign pairs are also stored in the same manner in a separate histogram. So for example in the case of five η bins, information on tag electrons would be stored in bins 1 through 5 and non-tag electrons in bins 6 through 10. This leads to a 10 by 10 matrix where only the diagonal and the entries above the diagonal are filled, since the order of the two electrons is arbitrary and therefore the electron in the lower bin can be selected first.

The number of same-sign events expected in one entry of the histogram $N_{ss}\,(i,j)$ at η bins i and j for the first and second electron respectively is given by

$$N_{ss}\,(i,j) = (\lambda\,(i) + \lambda\,(j))\,N\,(i,j) - O\left(\lambda^2\right)\,, \qquad (i \leq j)\,, \tag{7.9}$$

with $N(i,j)$ being the total number of events with one electron in bin i and the other in bin j and $\lambda\,(i)$ being the misidentification probability of an electron in a bin i. There will be mixed quadratic terms of the $\lambda(i)$ where both electrons are charge misidentified contributing to the value of N_{ss}, but since one is dealing with misidentification rates in the order of 10^{-2} or 10^{-3} these contributions are neglected.

Since the number of same sign events can be rather small a Gaussian approximation is not sufficient. It is therefore assumed that N_{ss} is distributed according to Poisson statistics:

$$N_{ss}\,(i,j) \sim \mathsf{P}\left((\lambda(i) + \lambda(j))\,N\,(i,j)\right) \equiv \mathsf{P}\left(\mu\,(i,j)\right) \tag{7.10}$$

The probability density function of the Poisson distribution is given by

$$f(n\,|\,\mu) = \frac{\mu^n}{n!}\,e^{-\mu}\,. \tag{7.11}$$

So a likelihood function can be constructed that assigns a value of likelihood to a set of parameters $\lambda(i)$ under the condition of an observed number of events $N(i,j)$ and same sign events $N_{ss}(i,j)$.

$$L(\lambda\,|\,N_{ss}, N) = \prod_{k,l} f\left(N_{ss}(k,l)\,|\,\mu(k,l)\right) = \prod_{k,l} \frac{\mu(k,l)^{N_{ss}(k,l)}}{N_{ss}(k,l)\,!}\,e^{\mu(k,l)} \tag{7.12}$$

Maximizing this likelihood function or equivalently its logarithm for the given set of parameters λ is a common technique and is known under the name Maximum-Log-Likelihood method [22, 23]. The maximum finder algorithm will yield the misidentification rates as well as their statistical errors for which the observed outcome is the most likely one. The logarithm of equation 7.12 is easily calculated as

$$\ln L(\lambda\,|\,\ldots) = -\sum_{k,l} \ln N_{ss}(k,l)! + \sum_{k,l} \left(N_{ss}(k,l)\,\ln\mu(k,l) - \mu(k,l)\right)\,, \tag{7.13}$$

and consists of a constant term that does not depend on $\mu(k,l)$ and a term depending on $\mu(k,l)$ and therefore on the set of λ. For the calculation of the maximum, the constant term is of no importance. Therefore the function to maximize is given by

$$L'(\lambda\,|\,\ldots) = \sum_{k,l} \left[N_{ss}(k,l)\,\ln\left(\lambda(k) + \lambda(l)\right) - N(k,l)\left(\lambda(k) + \lambda(l)\right)\right]\,. \tag{7.14}$$

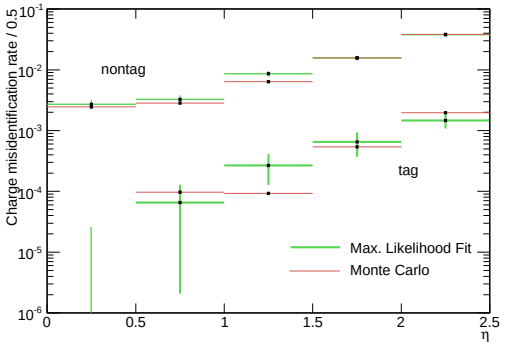

Figure 7.1: Charge misidentification rates for tag (t) and non-tag ($\bar{t}$) electrons as determined from Monte Carlo information and the maximum likelihood method.

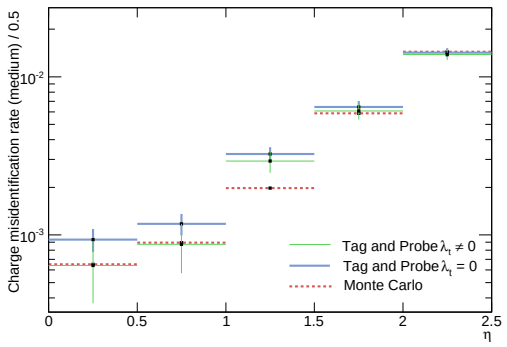

Figure 7.2: Charge misidentification rates for probe electrons (here medium electrons) as determined from Monte Carlo information and the tag-and-probe method with and without taking into account the tag misidentification rates.

The computer code MINUIT [24] was used to perform the maximization and the accompanying program MINOS was utilized to calculate the 1σ errors. The resulting values for the misidentification rates of the tag electrons and the non-tag electron are shown in table 7.3 together with their asymmetric 1σ errors. The tag electron charge misidentification rate in the first bin between the absolute η values 0 and 0.5 needs special mentioning. There are no observed same sign events in this bin, so the maximum likelihood fit yields a very low value of $1.038 \cdot 10^{-11}$, which can be treated as zero for all purposes of this analysis. Very interesting is the error estimate. It shows that a value of up to $2.36 \cdot 10^{-5}$ for the tag charge misidentification is compatible with the observed numbers of same sign events to a degree of confidence of 68%.

The plot in figure 7.1 summarizes the results of the maximum likelihood fit in graphical form. It shows the results for the tag and non-tag charge misidentification rates as

Table 7.3: Results of the maximum likelihood fit for the tag and non-tag charge misidentification rates in the $Z \to ee$ sample in five η bins. Tag electrons are tight electrons with an additional requirement of no additional reconstructed tracks within a distance of $\Delta R = 0.1$. Non-tag electrons are medium electrons that do not fulfill the tag requirements.

η bin	tag: $\lambda_t \,/\, 10^{-3}$		non-tag: $\lambda_{\bar{t}} \,/\, 10^{-3}$	
$0 \leq \eta < 0.5$	$0.00\ldots$	$^{+0.02}/_{—}$	2.71	$^{+0.51}/_{-0.46}$
$0.5 \leq \eta < 1.0$	0.07	$^{+0.08}/_{-0.05}$	3.27	$^{+0.56}/_{-0.51}$
$1.0 \leq \eta < 1.5$	0.27	$^{+0.16}/_{-0.12}$	8.63	$^{+0.93}/_{-0.87}$
$1.5 \leq \eta < 2.0$	0.65	$^{+0.31}/_{-0.25}$	15.69	$^{+1.38}/_{-1.31}$
$2.0 \leq \eta < 2.5$	1.46	$^{+0.41}/_{-0.35}$	38.04	$^{+2.27}/_{-2.19}$

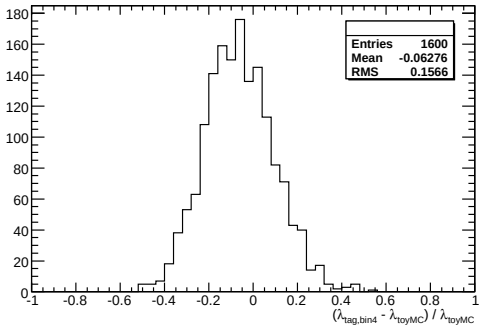

Figure 7.3: Distribution of the fit results around the truth input parameter value in units of the truth value.

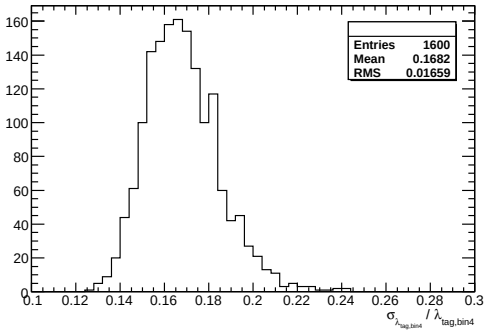

Figure 7.4: Distribution of the relative errors of the maximum likelihood fit results. The mean value is in agreement with the RMS value of the distribution of fit values in figure 7.3.

calculated with the maximum likelihood method compared to the values obtained by looking at the Monte Carlo information in the sample. Figure 7.2 shows the charge misidentification rates for medium electrons as obtained from Monte Carlo information and the tag-and-probe method for the two cases of neglecting λ_t or taking the tag misidentification rates obtained from the maximum likelihood fit into account.

7.4 Verification of the Fit Algorithm with a Toy Monte Carlo

In order to verify the robustness of the fit, a toy Monte Carlo model was employed. From the $Z \rightarrow ee$ sample the η distribution within the 10 by 10 bin histogram was determined. Now two electron events were generated according to this η distribution. Additionally the electrons were assigned the property of being correctly or misidentified according to a given value of charge misidentification probability. This way it was possible to generate a large number of events within a short amount of time and to test the fit algorithm with respect to its mean and error estimates. The experiment was repeated 1600 times with 200000 events generated each time. Figure 7.3 shows the distribution of the relative deviation of the fit values from the input Monte Carlo parameter for the charge misidentification rate. The distribution is centered around the truth input value and its mean value shows good agreement. The distribution of the relative error is shown in figure 7.4. The mean value of the relative errors agrees with the RMS value of the distribution of the relative deviation from the truth value, which shows that the errors given by the fitting algorithm are indeed sensible values. The difference between the mean value of the distribution of the relative deviation is much less than the relative error. Therefore, in a one measurement experiment, where there is only one sample at hand the error in the misidentification rate determined in such a way is dominated by statistics and not by the method.

8 Conclusions

Reconstructed electron objects at ATLAS consist of a track and a cluster in the electromagnetic calorimeter. Information from both detector components is merged into the reconstructed electron object. Therefore electron charge misidentification is not solely an issue of the detector hardware performance but depends heavily on the offline reconstruction process, where a track and a cluster are matched. It was shown in subsection 6.2.4 that only by considering the detector hardware performance as estimated by [4] one is led to a very optimistic estimation of the charge misidentification rate. The rate seen in full physics samples is higher. Especially for electrons with a transverse momentum below 500 GeV the charge misidentification rate would be underestimated by about one order of magnitude, if only the resolution of the track curvature measurement would be considered as source of electron charge misidentification. The dependence of the charge misidentification rate on the pseudorapidity η (see figure 5.2) leads to the assumption that the interaction of the electrons with the detector material plays an important part. Looking at the Monte Carlo information in a physics sample reveals that charge misidentified electrons seem to suffer more heavily from bremsstrahlung than the average electron, or put the other way around: Electrons that heavily suffer from bremsstrahlung on their way through the detector are more likely to be charge misidentified. The reason for this observation seems to lie in the fact that bremsstrahlung photons with high enough energy can convert within the detector material and the resulting electron pair can give rise to additional tracks in the Inner Detector and these tracks can prohibit the unambiguous association of a calorimeter cluster to a track. This mechanism of charge misidentification was examined in chapter 6. It was shown that in many cases it is indeed the track belonging to a conversion electron that is associated to the electromagnetic calorimeter cluster and not the track of the electron coming directly from the interaction. Again, up to a transverse momentum of about 500 GeV this seems to be the dominating source of electron charge misidentification, while at higher transverse momenta the finite detector resolution seems to be the primary source of electron charge misidentification.

The question important for physics analysis is if it is possible to reduce the charge misidentification rate without an unreasonable penalty in reconstruction efficiency. On the grounds of the results in sections 6.1 and 6.2, section 6.3 describes some possible cuts and criteria in order to reduce the electron charge misidentification rate in reconstructed data. The most effective measures turned out to be a cut requiring the electron track to be isolated from adjacent tracks within a certain distance in η and ϕ and a cut on the transverse impact parameter d_0. With the first method a reduction of about 80% of the charge misidentification rate can be accomplished with a cut efficiency of about 80% in the case of $Z \rightarrow ee$ processes. The cut on the transverse impact parameter seems to be even more powerful as it seems to allow a reduction of charge misidentification rate beyond 90% with a cut efficiency of more than 80%. For early data however the transverse impact parameter might not be the best value to cut on, since it is subject to

a comprehensive knowledge of detector alignment.

The final chapter of this thesis, chapter 7 dealt with the question on how to measure the charge misidentification rate in real data. A tag-and-probe ansatz was chosen. Here it is important to have a class of tag electrons, whose charge misidentification rate is much lower than the one of the probe electrons, which is to be determined. As tags, electrons with sufficient track isolation were chosen. For a first estimate their charge misidentification rate was neglected. In order to further improve the results, a maximum likelihood method was employed to determine the charge misidentification rate of the tag electrons. The results from the tag-and-probe method were in agreement with the numbers obtained from Monte Carlo information. Therefore the tag-and-probe method seems to be a suitable method for determining the actual electron charge misidentification rate from real data, when they become available in 2009.

Bibliography

[1] ATLAS public website. URL `http://www.atlas.ch`.

[2] LHC public website. URL `http://lhc.web.cern.ch/lhc`.

[3] ATLAS Collaboration. ATLAS detector and physics performance technical design report. *Vol. I, ATLAS TDR*, (ATLAS TDR 14. CERN/LHCC 99-14), 1999.

[4] ATLAS Collaboration. The ATLAS experiment at the CERN Large Hadron Collider. *JINST*, 3, August 2008.

[5] G. Gagliardi. The ATLAS pixel detector: A hundred million channels vertex detector for LHC. *Nuclear Instruments and Methods in Physics Research, A*, 546 (1-2F):67–71, 2005. doi: doi:10.1016/j.nima.2005.03.111.

[6] L. C. L. Yuan, C. L. Wang, H. Uto, and S. Prunster. Energy dependence of x-ray transition radiation from ultrarelativistic charged particles. *Physics Letters B*, 31: 603–605, 1970.

[7] T. Cornelissen, M. Elsing, S. Fleischmann, W. Liebig, E. Moyse, and A. Salzburger. Concepts, design and implementation of the ATLAS New Tracking (NEWT). Technical Report ATL-SOFT-PUB-2007-007. ATL-COM-SOFT-2007-002, CERN, Geneva, March 2007.

[8] M. Aharrouche and ATLAS Electromagnetic Barrel C. Collaboration. Energy linearity and resolution of the atlas electromagnetic barrel calorimeter in an electron test-beam. *NUCL.INSTRUM.METH.A*, 568:601, 2006. URL `http://www.citebase.org/abstract?id=oai:arXiv.org:physics/0608012`.

[9] ATLAS Collaboration. ATLAS computing technical design report. *ATLAS TDR*, (ATLAS TDR 17. CERN-LHCC-2005-022), 2005. URL `http://doc.cern.ch/ /archive/electronic/cern/preprints/lhcc/public/lhcc-2005-022.pdf`.

[10] ATLAS Collaboration. ATLAS computing workbook, . URL `http://twiki.cern.ch/twiki/bin/view/Atlas/WorkBookAthenaFramework`.

[11] G. Barrand et al. Gaudi – a software architecture and framework for building hep data processing applications. *Computer Physics Communications*, 140:45–55, 2001.

[12] Ganga public website. URL `http://ganga.web.cern.ch/ganga`.

[13] K. Harrison et al. Ganga: A grid user interface for distributed analysis. In S. Cox, editor, *Proceedings of the UK e-Scinece All Hands Meeting*, pages 518–525, September 2006.

[14] ROOT an object-oriented data analysis framework. URL `http://root.cern.ch`.

[15] C. Amsler et al. Review of Particle Physics. *Phys. Lett. B*, 667(1), 2008.

[16] W. Lavrijsen. PyRoot public website. URL `http://wlav.web.cern.ch/wlav/pyroot`.

[17] ATLAS egamma performance group. Electron reconstruction. URL `https://twiki.cern.ch/twiki/bin/viewauth/AtlasProtected/ElectronReconstruction`. (Last accessed: October 1st, 2008).

[18] ATLAS Collaboration. Inner detector geometry model, . URL `https://twiki.cern.ch/twiki/bin/view/Atlas/InDetMaterial`. (Last accessed: October 2nd, 2008).

[19] E. Lohrmann. *Hochenergiephysik*. B. G. Teubner, 2nd edition, 1981.

[20] W. Heitler. *The Quantum Theory of Radiation*. Oxford University Press, 3rd edition, 1954.

[21] ATLAS Collaboration. Expected performance of the ATLAS experiment, detector trigger and physics. Technical Report CERN-OPEN-2008-020, CERN, Geneva, 2008. to appear.

[22] F. James. *Statistical Methods in Experimental Physics*. World Scientific, 2nd edition, 2006.

[23] E. Kreyszig. *Statistische Methoden und Ihre Anwendungen*. Vandenhoeck & Ruprecht, 1965.

[24] F. James and M. Roos. MINUIT: a system for function minimization and analysis of the parameter errors and corrections. oai:cds.cern.ch:310399. *Comput. Phys. Commun.*, 10(CERN-DD-75-20):343–367. 38 p, July 1975.

Danksagungen

Es bleibt mir noch, mich an dieser Stelle bei all jenen zu bedanken, ohne die das Zustandekommen dieser Arbeit nicht möglich gewesen wäre:

- Prof. Dr. Dorothee Schaile für das in mich gesetzte Vertrauen und die Aufnahme an ihrem Lehrstuhl, sowie für die Erstellung des Erstgutachtens.
- Prof. Dr. Martin Faessler für die Erstellung des Zweitgutachtens.
- Ganz besonders möchte ich mich bei PD Dr. Raimund Ströhmer für die Betreuung meiner Arbeit und die zahlreichen Anregungen bedanken, sowie für die stets geduldige Beantwortung all meiner Fragen und die immer offene Tür zu seinem Büro.
- Dr. Cédric Serfon, Julien de Graat und Christian Kummer für die nette Aufnahme im nunmehr gemeinsamen Büro und die mehr als angenehme Arbeitsatmosphäre.
- Julien de Graat für das Korrekturlesen dieser Arbeit.
- Frau Herta Franz für ein stets freundliches Wort und den zuletzt aufmunternden Zuspruch.
- Dr. Johannes Elmsheuser für seine immer gewährte Unterstützung insbesondere bei meinem Kampf mit ATHENA und Ganga.
- Prof. Dr. Dorothee Schaile, PD Dr. Raimund Ströhmer, Dr. Marie-Hélène Genest, Dr. Cédric Serfon, Julien de Graat, Christian Kummer und Jonas Will für die vielen Anregungen in unserem wöchentlichen SUSY-Meeting.
- Dr. Gernot Krobath für die angeregten und interessanten Diskussionen.
- Markus Lichtenecker für die netten Besuche in unserem Büro und die unterstützenden Worte.
- allen bisher noch nicht genannten Mitgliedern des Lehrstuhls:
  Prof. Dr. Otmar Biebel, Dr. Philippe Calfayan, Günter Duckeck, Johannes Ebke, Albert Engl, Dr. Cristina Galea, Alexander Grohsjean, Petra Haefner, Klaus Herrmann, Dr. Ralf Hertenberger, Dr. John Kennedy, Dr. Tariq Mahmoud, Dr. Raphael Mameghani, Dr. Doris Merkl, Christoph Mitterer, Thomas Müller, PD Dr. Thomas Nunnemann, Dr. Felix Rauscher, Benjamin Ruckert, Dr. Michiel Sanders, Dr. Matthias Schott, Attila Varga für die freundliche Aufnahme und den stets freundschaftlichen Umgang.

- Kirsten Gratz für die Begleitung durch die letzten Jahre und die stete Unterstützung bei all meinen Vorhaben.
- meinen Eltern Helga und Bernd und meiner Schwester Beatrice für die immer uneingeschränkte Unterstützung und Zuversicht.
- nicht zuletzt danke ich all meinen Lehrern, die mich an ihrem Wissen und ihrer Begeisterung teilhaben ließen. An ihrer Stelle seien stellvertretend genannt: Herr Erhard Beck, Herr Otto Midasch, Herr Heer, ...

Erklärung

Ich versichere hiermit, die vorliegende Arbeit selbständig verfasst zu haben und keine anderen als die angegebenen Quellen und Hilfsmittel verwendet zu haben.

Michael Wichmann

München, den 25. November 2008